Cavity-QED Implementations for Distributive Quantum Computation

Hamzah M. Shokeir

Supervised by: Prof M.Keller

A thesis presented for the degree of

Master of Philosophy

Department of Mathematical and Physical Sciences

University of Sussex

April 2020

***Recorded Doc Brown**: No, no, no, no, no, this sucker's electrical, but I need a nuclear reaction to generate the 1.21 gigawatts of electricity I need...*

***Doc Brown in 55'**: 1.21 GIGAWATTS!!?? 1.21 GIGAWATTS!?... Great scot. (Stumbles out of the room)*

***Marty**: What the hell is a gigawatt?!*

-Back to the Future, Part I.

花に捧げる

Acknowledgements

This work would not have materialised had it not been for the generous support of my supervisor Matthias Keller who welcomed me to ITCM in September 2017. I thank you for being particularly patient with me and supervising me on this journey. ITCM would not be what it is without the scientists who comprise it, I extend my gratitude to Xavi Fernandez Gonzalvo who took the time to have a number of meaningful discussions and was always such a pleasure to chat and laugh with. I thank Sam Snowden who was always available for support weather it be on long nights doing coursework or petty mathematical queries, the group is lucky to have such diligence. Tom Walker, you're a scientist in every sense of the definition thank you for your help and all the best in Freiburg working with Tobias Schatz. I thank Samir who assisted me a great deal in debugg the PDH simulations. Laura, thanks for being a model example to follow and for all your support. Costas, thanks for the cigarettes (and much more of course). Thank you Callan, having atleast one normal, sane person in the group made all the difference, great things are coming your way. Thank you Ezra Kassa and Hiroki Takahashi for getting me started in the lab. and Alan Butler for his craftsman skills. Thanks Corentin for being a pleasure to be around, your hard work will pay off. To all the newcomers; Travers, David and Graham I wish you all the best.
The decision to terminate my studies early and convert my research from PhD to MPhil was one not taken lightly but one that was the best decision for myself at the time. Outside the lab I owe a number of thanks to friends who helped me through this journey. , your genuine warmth and kindness is so rare, I'm lucky to call you my friend. , thanks for helping me realise that a healthy life is a balanced life. To the members of Sussex Friends of Palestine, the resistance and fight for social justice continues. Thank you , 2019 would not have been the same had I not seen your doppelganger on the 25 bus that morning of October 2nd 18'. Thank you for welcoming me into your home. And , I am extremely lucky to have met you and to be able to call you more than just a friend. To all the above mentioned, thank you for giving me something I'd never thought I'd find in Brighton; a family.
To the friends outside of Brighton I owe a lot to the following: , you've been there since the beginning at Queen Mary, thanks for being the older brother who was always there for me. Thank you dear for accompanying me on adventures, from Montreal to Gozo. Thank you who supported me from Lancaster to Brighton, I hope you're well, you deserve every ounce of success. And of course , and who have been there through thick and thin.
The entire journey would not have been possible without the help and support of my father. Nor would I have decided to peruse a life as a scientist if it wasn't for my mother, thank you both. And last (by no means least) I thank my sister who has been my number one fan. This thesis is dedicated to you. May the world be a better place for you and your children.

Declaration

I hereby declare that this thesis has not been and will not be, submitted in whole or in part to another University for the award of any other degree.

Signature:

Hamzah M. Shokeir

May 2020

UNIVERSITY OF SUSSEX

Hamzah M. Shokeir, Master of Philosophy

Cavity QED Implementations for Distributive Quantum Computation

Abstract

The coupling of a single ion to an optical cavity is a promising route towards scalable quantum technologies. This study presents the design, initial construction and simulations of two different ion traps for quantum computation with novel capabilities. The first system is an end cap system that utilises Fabry Perot cavities formed by the facets of fibres. The small mode volumes (cavity length $\sim 300\,\mu$m) of the fibre cavities are ideal to achieve high cooperativity and coupling strength. This trap features the novel ability to mechanically adjust the position of the ion by perturbing/distorting the trapping potential with grounded side electrodes. A capability crucial to maximising the ion-cavity coupling. The design incorporates a number of improvements over the previous iteration by Takahashi et al. such as increased optical access, increased mode matching and improved mechanical stability of the cavity. To verify and test the design modifications; Pound-Drever-Hall cavity locking was set up.

The test set up failed to lock to an error signal due to a mechanically unstable translation stage. The other design presented is a linear micro trap intended to trap strings of ions and does not use fibre based cavities. This design features multiple different regions reserved for storage, computation and communication and aims to implement a shuttling scheme that will allow the selective loading of single ions from a reservoir of ions into the desired regions. The fabrication process would utilise methods in microfabrication. Simulations of the trapping dynamics were used to optimise the electrode geometries and splitting protocol.

Conference Contributions

Towards Deterministic Entanglement of Trapped Ion Systems

Hamzah M. Shokeir, Matthias Keller

Poster presentation at biannual Quantum, Atomic, and Molecular Physics (QuAMP 2019) Conference, Birmingham University, UK, September 2019.

Awards

Alan Gibson Poster Prize, jointly awarded by the QQQ and QEP.

For: Towards deterministic entanglement of trapped ion systems.

Contents

List of Figures **10**

1 Introduction **11**

1.1 Requirements of a Quantum Computer 11

1.2 Approaches to Quantum Networks 14

1.3 Coupling Ions to Optical Cavities 17

1.4 Structure of Thesis 19

2 A Novel End Cap Paul Trap **20**

2.1 Introduction 20

2.2 Ion Trapping Theory 21

2.2.1 Pseudopotential Approximation 24

2.3 Designing an End Cap Trap 25

2.3.1 Previous Designs 25

2.3.2 The New Design 27

2.3.3 Electrode Assemblies and Insertion Process 29

2.3.4 Radial Adjustment of the Ion Position 33

2.4 Simulation 34

2.4.1 Results 35

3 Implementing Fibre Cavities for cQED **38**

3.1 Introduction 38

3.2 Optical Cavities 38

3.3 Benefits of Fibre Cavities 47

3.4 Developing a Stable Fibre Cavity System 49

3.4.1 Pound-Drever-Hall Locking Scheme 49

3.5 Drawbacks of Fibre Cavities 54

3.5.1 The Setup 55

3.5.2 Generating an Error Signal in Transmission 55

3.5.3 Attempting to Lock in Transmission 57
3.6 Conclusion 62

4 A Linear Microfabricated Trap 63
4.1 Introduction 63
4.2 Proposed Design 64
4.3 rf Simulations 66
4.3.1 rf Electrode Geometry 66
4.3.2 Positioning the Ion with rf 69
4.4 Axial Trapping Dynamics 71
4.4.1 dc Electrode Geometry and Trapping Dynamics 72
4.5 Splitting an Ion Crystal 74
4.5.1 The Quartic Component 75
4.5.2 Molecular Dynamics Simulations 78

5 Conclusion & Outlook 80

List of Figures

1 Two node remote entanglement scheme 17
2 Endcap electrode structure 19
3 The stable trapping region 23
4 Ideal endcap Paul trap 24
5 Closeup of electrode assembly 26
6 New design of an endcap ion trap 28
7 cross section of new and old trap designs 29
8 Insertion set up 31
9 concentricity of fibre-electrode assembly 32
10 positioning ion with electrodes 33
11 Pseudopotentials in both axial and radial directions 34
12 Shifting of pseudopotential min 35
13 Secular frequencies of shifted pseudopotentials 36
14 pseudopotential map of trap cross section 36
15 The Fabry Perot optical cavity 39
16 Cavity transmission peaks 42
17 Dips in reflection due to impedance matching 44
18 Fundamental Gaussian mode 45
19 Cavity stability diagram 46
20 Fibre cavity and a GRIN assembly cavity 48
21 Phase relation for input and output light of a cavity 51
22 PDH error signal in reflection 53
23 Schematic of a PDH system 54
24 The test set up mounting structure 55
25 The generated error signal in transmission 56
26 Optimised simulated error signals 57
27 Cavity signal prior to engaging lock 58
28 Delayed signal from mixer and PI 60

29 Improved cavity signal prior to engaging lock 61
30 CAD of linear microtrap 65
31 Axial electrode arrangement 66
32 Electrode ion separation and effect on potential 67
33 Schematic of cross section of the electrode structure 67
34 RF electrode-ion separation on secular frequency 68
35 Reduction of rf electrode thickness 68
36 Varying position of potential minimum 70
37 2D slice of potential distribution when varying amplitudes on two electrodes 70
38 Secular frequency when varying electrode amplitude 71
39 Schematic of the simulated electrode configuration 73
40 The effect of varying the electrode width on secular frequency and trap depth 73
41 The effect of varying the electrode retraction on secular frequency and trap depth 74
42 Potential evolution, quadratic to quartic 76
43 Sum of potentials from three electrodes 77
44 Quartic component at the critical point for varying electrode dimensions 78
45 Splitting of two ions in a quartic potential 79

1 Introduction

1.1 Requirements of a Quantum Computer

One of the earliest proposals for an algorithm that would solve problems faster than a conventional computer was Shor's algorithm [1] in which a large integer N can be decomposed into it's constituent prime factors. A quantum analogous Turing Machine (aka a quantum computer) would solve said problem and others exponentially faster than a classical computer. However, it wasn't until 1996 at IBM's research division when David Di'Vincenzo outlined a set of requirements that would suffice to create a physical quantum computer [2]. They include:

1) A scalable physical system with well characterised qubits.

2) The ability to initialise and prepare the state of the qubits to simple fiducial states.

3) Controlled unitary transformations which would enable a "universal" set of quantum gates.

4) Long decoherence times, (larger than the gate operation time,(a quoted decoherence time of 1×10^6 times longer than the gate operation time)).

5) A qubit specific measurement capability.

The 'qubits' being analogous to the 'bits' of the classical computer. Trapped ions have been demonstrated to be a suitable candidate meeting the first five requirements. Ions surpass other qubit species on a number of aspects such as qubit coherence times [3], readout fidelities of 99.99% [4] and the ability to be trapped for days [5].
Further outlined in Di'Vincenzo's paper was the advent for a quantum computer to communicate with other quantum computers potentially forming a type of 'quantum network' [6]. Such a network would not only enhance quantum computation but would

enhance the emerging fields of sensing [7], time keeping [8], cryptography [9] and communication. To envision a system that would facilitate both, two additional requirements were established, namely:

6) The ability to inter-convert stationary and flying qubits.

7) The ability to transmit flying qubits between distant locations.

Photons are often referend to as nature's communication qubit given their current use in long distance communication both in free space [10] and via optical fibre [11]. The natural counterpart to trapped ions are the photons they emit and given the ions capability to be entangled with the photon's parameters (such as polarisation and frequency) make trapped ions a more desirable candidate for a scalable quantum computer. However, the interactions that govern the exchange of ions to photons is inherently weak. The enhancement of this interaction would require placing the ion in an optical resonator.

From this emerges cavity quantum electrodynamics (cavity QED), in which the interaction of the ion/atom and the cavity field is reversible and the coupling of the two systems can be optimised to exceed the rate of decay of the irreversible process of the photons decaying from the cavity and the decay rate of the atom. Analogous models are seen in circuit QED in which Cooper pairs are coupled to superconducting strip line resonators. Cavity QED in the optical domain is particularly useful in quantum networking in which low temperature environments are not required and fibre optics can facilitate the exchange of photons over long distances. In recent years the development of high quality Fabry Perot optical cavity mirrors [12] enable the exploitation of the interaction between the ion and the modes that exist within the cavity. This interaction has been shown to produce single photons deterministically [13], a crucial step in realising a quantum network. Micro-cavities machined from the facets of optical fibres often referred to as fibre based Fabry Perot cavities (FFPC) have been a promising

component in the development of cavity QED systems.

In addition to the aforementioned aspects of trapped ions, other benefits include their inherent indistinguishability. Current standards in fabrication of other qubit species such as diamond nitrogen vacancy centres, quantum dots and superconducting qubits do not necessarily yield identical qubits which leads to issues in implementation, [14].

It is worth adding that within the wider context of the development of a scalable quantum computer, that the current dominating approach of which is being pursued by the likes of IBM and Google are superconducting qubits [15, 16]. Thus far, these systems have quickly rose to a successful standard in achieving a large number of qubits (53 as of 2019 [17]).

However, it has been noted that due to the conditions that these qubits require (namely the sub millikelvin temperatures that are provided by dilution refrigerators) further scaling these systems may pose to be technically challenging and thus this architecture may pose an issue towards scalability.

Creating a scalable system of qubits is an important step in realising a quantum computer. Whereas the dominating approach in the US has been superconducting qubits, in the UK trapped ions have been the favoured candidate. Two approaches have been perused; one entails creating a segmented array of multiple of ions in a CCD like architecture, dubbed as a quantum charge coupled device (QCCD). The other is a modular/networked approach in which individual traps are interconnected via optical links [18].

In the former; a device would typically house various segments reserved for different purposes such as memory or computation. The ions are transported by means of shuttling to their relevant regions. One of the earliest proposals for a two qubit quantum gate for trapped ions was developed by Cirac and Zoller [19] dubbed as the 'controlled-NOT gate'. More recently, two qubit ion trap gates with fidelities as high as 99.9 % have been achieved [20]. However, scaling a single QCCD devices pose a number of

difficulties such as heating and efficient scalability [21]. To this end, the latter of the two aforementioned means of scaling would be more suitable.

Trapped ions also feature the smallest ratio of entanglement generation time to entangled state coherence time (order of seconds) [22]. Neutral atoms are the closest in comparison with similar entanglement generation times to trapped ions but feature entanglement coherence times in the order of microseconds [23]. As the ratio increases, the overhead in resources (defined in [24] as the ratio squared) increases. These particular features make trapped ions favourable when implementing a scalable architecture based on entanglement schemes.

To this end, trapped ions have been proven to be a promising platform that meet all the requirements of Di'Vincenzo's criteria with algorithms on chains of up to 79 ions have been demonstrated [25]. Thus, a quantum network (QN) comprised of trapped ions would not only facilitate quantum computation but would also enable scalability in a distributive like scheme. A QN of such (or a quantum internet [6]), would use ions due to their long storage lifetimes as the stationary qubits dedicated to gate operations and photons to act as the flying qubit that facilitate state transfer and to act as communication channels. Further developing the exchange of information between the ion and the photon is of central importance in the development of a quantum network.

1.2 Approaches to Quantum Networks

Within the networked approach individual traps exist as a node or module [18]. Each module contains a manageable number of trapped ions and are interconnected via optical links. These optical channels carry the photons via optical fibres with little decoherence. However there exists some form of exponential decay of the photon due to scattering and absorption losses within the fibre. Classically, this has been circumvented with the use of a repeater that amplifies the signal. A quantum analogous repeater circumvents the no-cloning theorem [26] and has been the basis for a large scale QN

for communication. On the other hand, QNs that do not rely on quantum repeaters have been proposed for large scale computation. These form a distributive quantum computer with individual nodes working in parallel with other nodes.

Two key approaches to QN exist, the first scheme is of a deterministic approach first introduced in [27], their theoretical protocol outlines quantum transmission with unit probability. Their set-up consists of two separate atoms in optical cavities connected via a transmission line. Information of the internal state of an atom in one node is transferred to the optical state of the cavity mode, the time-symmetric photon is transferred via the transmission line (optical fibre) to the second node, the optical state of the photon in the second cavity is then mapped to the second atom. This deterministic proposal relies on strong coupling of the optical cavity to the atoms (discussed further in Chapter 2). Although strong coupling of a single ion to an optical cavity [28] and schemes of deterministic photon generation [29] have been demonstrated. Achieving a deterministic network of trapped ions has been technically challenging predominantly due to the requirement of high finesse optical cavities [30] and the small mode volumes required. Further details on the requirements of optical cavities are discussed in Chapter 3.

Alternatively, a probabilistic network is the second approach and is one that trades small mode volume optical cavities and the challenges that come with their implementation for longer operation times and lower efficiency. The entanglement scheme is repeated until a successful outcome is reached and hence unit efficiency is lost [31]. In the probabilistic scheme, entanglement is heralded by the detection of an external photon, this detection projects the two atoms into an entangled state.

Fig.1 demonstrates a similar scheme to one of the earlier demonstrations of a probabilistic network [32]. A cavity mediates a Raman transition with the use of a π-polarised laser pulse which drives the ion from its ground state ($S_{1/2}$) to the excited state ($P_{1/2}$), this generates orthogonally polarised σ cavity photons which are dependant on the

ion's state. The entangled state of the ion is $|\psi\rangle = (|0, \sigma^+\rangle + |1, \sigma^-\rangle)/\sqrt{2}$. The photons emerge from the cavities and depending on their polarisation enter the detectors. For photons of the same polarisation both leave the same port and either enter detector 1 or 2. For photons of different polarisation; 50% of cases one detector will indicate a measurement while during the other 50% both detectors will register a measurement. For the latter of the two cases, this event heralds the entanglement of the two ions and is in a state $|\psi\rangle = (|0, 1\rangle + |1, 0\rangle)/\sqrt{2}$. The schemes have been demonstrated to work with $^{40}Ca^+$ at a fidelity of 91%, [33]. The most recent demonstration of a heralded scheme yielded a fidelity of 94% without the use of an optical cavity [34].

In principle these schemes do not require cavities, however the use of optical cavities have shown to increase the fidelity of the process. The use of a cavity will enable the ion to be coupled to a particular mode of the cavity which will enable coherent control of the interaction and will greatly increase collection efficiency. For ions in free space, the desired photon could be emitted in all directions and only a small fraction of light is collected through a high numerical aperture lens and hence the collection efficiency is limited.

A recent milestone was demonstrated [33] in which tunable entanglement (control of the phase and amplitude of the entangled state) of a single calcium ion and a photon's polarisation in an optical cavity is demonstrated. The scheme shows that no coherent manipulation of the input state is necessary.

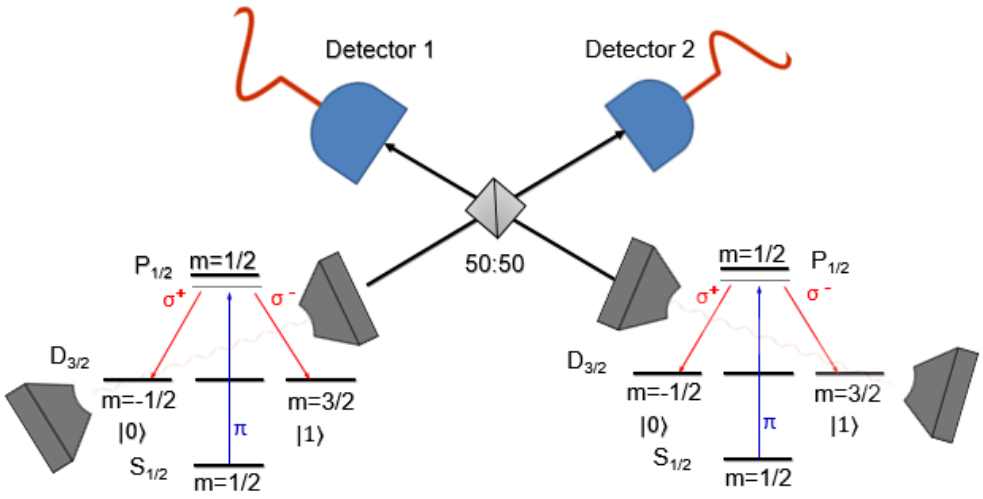

Detector 1 click	Detector 2 click	Photon State	Ion Entanglement
x	✓	$\|\sigma^+, \sigma^+\rangle$ or $\|\sigma^-, \sigma^-\rangle$	x
✓	x	$\|\sigma^+, \sigma^+\rangle$ or $\|\sigma^-, \sigma^-\rangle$	x
✓	✓	$\|\sigma^+, \sigma^-\rangle + \|\sigma^-, \sigma^+\rangle$	$\frac{1}{\sqrt{2}}(\|0,1\rangle + \|1,0\rangle)$

Figure 1: The simplest example of a quantum network consists of two ions linked by entangling the ion's state to the photon's polarisation. The two ions with a lambda scheme are each in an optical cavity, beam splitters (50:50) are used to filter two generated σ polarised photons. A detection is made, heralding successful entanglement.

1.3 Coupling Ions to Optical Cavities

Deterministic entanglement has been a long elusive goal with trapped ions. One route towards this is by having good atom-cavity cooperativity or by reaching the strong coupling limit in which the atom-photon coupling greatly exceeds both the non-resonant decay of the atom and the photon decay rate of the cavity. Being in the strong coupling regime would increase efficiency and coherence of the system. Recently the achievement of strong coupling between a single calcium ion in an optical fibre cavity [28] suggests that such a goal is within near reach. The design used by Takahashi et al. is an end cap style Paul trap, in which the cavity is incorporated within the main rf trapping electrodes. The system also allows mechanical translation of the cavity such that an optimal overlap between the cavity mode and the ion could be achieved axially whilst

allowing for precise positioning of the ion radially in the order of micrometres. Although the need for such fine adjustment is crucial in optimising the coupling it adds a level of complexity specific to this system. Nonetheless, due to the scale of the cavity and their proximity to the ion, this novel design allows for a minimal mode volume (a key parameter in maximising the coupling strength). To overcome the issue of dielectric interference of the cavity surface with the trapping field, the fibre cavities were retracted into the electrodes by $5 - 10\mu m$. It is currently the only ion trap system to achieve strong coupling to an optical cavity. Unlike other fibre based cavity QED traps, the cavities used in [28] feature a high degree of rotation symmetry which leads to low birefringence. Other Paul traps that have incorporated fibre cavities with the aim of achieving strong coupling have demonstrated the spatially dependant coupling of the ion to the cavity field [35]. In this trap, the arrangement of the cavity and the electrodes yield significantly less optical access to the ion in the z-y plane (15°) [36] than in [28]. Similar traps that feature fibre based cavities with mirror coatings for ultraviolet wavelengths have been reported to show little to no degradation over the course of 9 months but feature a large photon cavity decay rate, limiting the system to the weak coupling regime [37].

A vastly different trap to the end cap Paul trap used by Takahashi et al. is a linear trap. These particular systems are useful for trapping multiple ions in the form of stings. Linear traps combined with optical cavities have been implemented to demonstrate coherent control of the ion's emission into a single spatial mode and the ability to control the temporal shape of the emitted photons, [38]. In this particular set-up, the cavity is placed in the dc endcap electrodes and features a length of 5.3 mm which yields a large mode volume, the cavity and ion are weakly coupled.

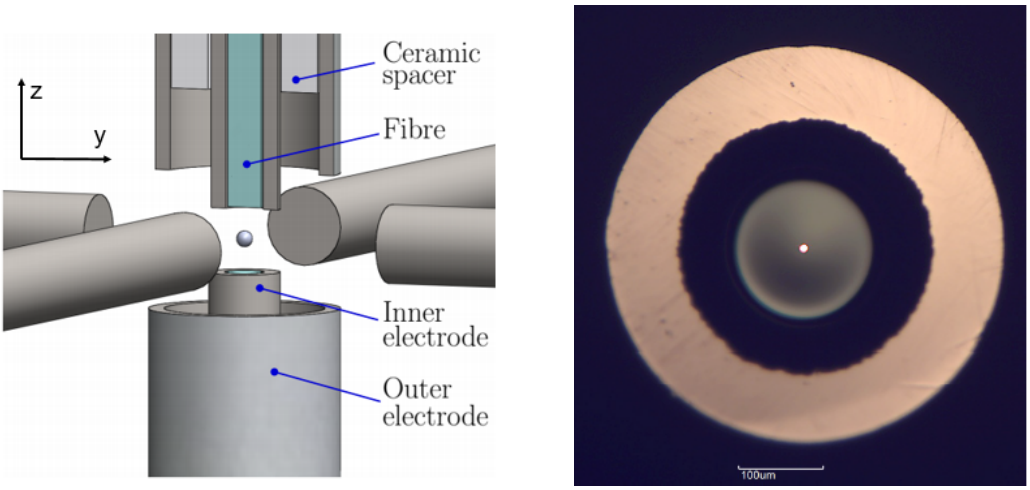

(a) (b)

Figure 2: a) The electrode configuration of the system used by Takahashi et al. A pair of electrodes with incorporated fibre cavities (upper electrode shows cross section to highlight internal structure), surrounded by four electrodes on the radial plane [39]. b) Microscope image of electrode cavity assembly.

1.4 Structure of Thesis

The study presented in this thesis looks at the development of a single node of a trapped ion cavity QED processor. Chapter 2 discusses a novel proposed design of an endcap style Paul trap based on a previous successful design that achieved strong coupling [28]. It explores a novel method of precisely positioning the ion with respect to the cavity mode by distorting the trapping potential. In chapter 3 a number of issues during the construction of a test system that are inherent to the implementation of fibre based cavities in a cQED set-up are uncovered, such issues concern the structural stability and optical limitations. In chapter 4 an alternate system is proposed. A linear style trap without the use of fibre cavities that rely on methods of microfabrication. The proposed alternative employs a shuttling and splitting based scheme in which separate regions of the linear trap are reserved for tasks such as loading, computation and communication.

2 A Novel End Cap Paul Trap

2.1 Introduction

A key development in atomic precision spectroscopy is the ion trap. The ability to address individual particles with great precision and for long periods of time further allowed the development in other fields such mass spectrometry and in precision time keeping (atomic clocks). As highlighted in Section 1.2 trapped ions are now a strong candidate for a scalable quantum computer. The two main types of ion traps are the Penning trap and the Paul trap, both of which are being used to develop scalable quantum computing devices. However, this thesis will focus on the latter.

The design used by Takahashi et al. [28] was the result of multiple iterations and was developed over the course of years. An improved version of the end cap style system used in [28] is discussed later in this chapter, with the objective of improving the system's performance. The system in [28] successfully achieved a coupling strength of $g_0 = 2\pi(15.1 \pm 0.1)$ MHz, an atomic decay rate $\gamma = 2\pi(11.5)$ MHz and a cavity decay rate of $\kappa = 2\pi(4.1 \pm 0.1)$ MHz which satisfies the condition for strong coupling, namely $g > \gamma, \kappa$. Various design limitations of this system are pointed out and the possible design flaws that led to this are discussed. The new design addresses elements concerning the mechanical stability of the cavity, optical access, limited coupling to the desired mode and incorporating a novel feature in controlling the ion's position. The goal is to increase the coupling strength and to demonstrate a deterministic scheme. Prior to this discussion some basic ion trapping theory is outlined and later simulations results done via a finite element simulation model (COMSOL Multiphysics) that highlight the new trap's capability in controlling the ion's position are presented.

2.2 Ion Trapping Theory

The purpose of this subchapter is out outline some of the background theory associated with ion trapping. The equations derived will be useful in determining the ideal trap geometry for an improved endcap Paul trap as well as understanding some of the dynamics of ion trapping which will be used in Chapter 4.

Earnshaw's theorem states that: "A charge acted on by electrostatic forces cannot rest in stable equilibrium in an electric field". This theorem is a direct consequence of the fact that an electric field has no divergence in a region with no charge density. Maxwell's equation reads $\vec{\bigtriangledown}\mathbf{D} = \rho_{freespace}$, assuming $\rho_{freespace} = 0$ the divergence of zero suggests that there are no sources or sinks. A static field alone will be incapable in trapping a charged particle in three dimensions, as will be made clear later, the Paul trap [40] was a means around this.

Beginning with solving Laplace's equation ($\vec{\bigtriangledown}^2\phi = 0$) at the lowest order expansion the non-static potential can be expressed as

$$\phi = \alpha x^2 + \beta y^2 + \gamma z^2. \tag{1}$$

By choosing constants $\alpha + \beta + \gamma = 0$ appropriately, the potential can be reduced to

$$\phi = k(r^2 - 2z^2). \tag{2}$$

In a cylindrically symmetrical system where r is the radial dimension $(x^2 + y^2)$. The potential is comprised of a static dc field and an oscillating rf. The rf voltage takes the form $V = V_0 \cdot \cos(\Omega t)$. When boundary conditions are incorporated for an end cap trap (Fig. 4) the potential can be simply expressed as

$$\phi = \frac{-U_{dc} + V_{ac} \cdot \cos(\Omega t)}{(2z_0^2 + r^2)}(r^2 - 2z^2). \tag{3}$$

Where U_{dc} are the dc potentials and V_{ac} are the rf potentials and Ω is the frequency of the rf. The equations of motion in the radial and axial degrees can be expressed as

$$\vec{F} = m\ddot{\vec{x}} = -e \bigtriangledown \vec{\phi}, \tag{4}$$

substituting equation (3) and (4), we obtain a result that can be expressed as

$$F_r = \frac{2e}{r_0^2 + 2z_0^2} U_{dc} + V_{ac} \cos(\Omega t) \cdot r. \tag{5}$$

This is a form of the Mathieu equation and can be expressed as:

$$\frac{d^2 r}{d\tau^2} + (a - 2q\cos(2\tau))r = 0, \tag{6}$$

where $\tau = \frac{\Omega t}{2}$ and the two parameters a and q govern the dynamics of the trapping behaviour. A set of solutions that govern the stable motion of our ion, (i.e. when the ion is bound to our potential) can be found, these are

$$a_z = -2a_r = \frac{-16eU_{dc}}{m\Omega^2(r_0^2 + 2z_0^2)}, \tag{7}$$

$$q_z = -2q_r = \frac{-8eV_{ac}}{m\Omega^2(r_0^2 + 2z_0^2)}. \tag{8}$$

Plotting a and q for the axial and radial directions gives us the stability diagram which highlights the boundary in which the ion's motion exists stably.

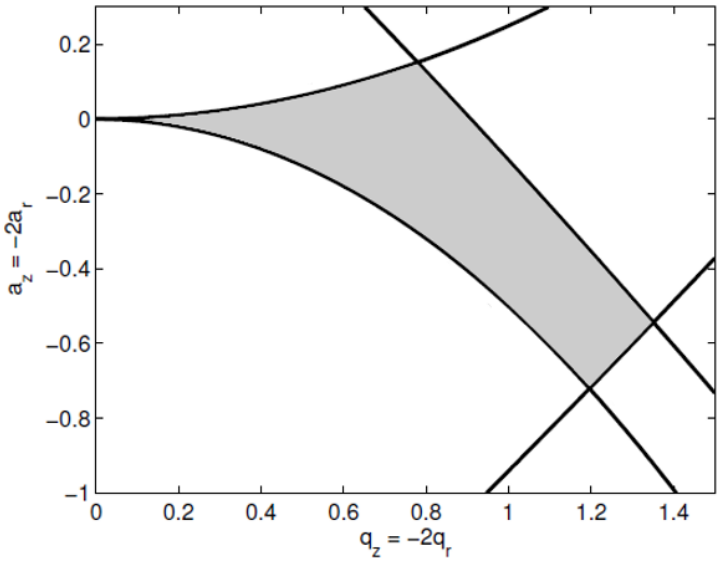

Figure 3: The stable trapping region for an ideal Paul trap as a function of dc amplitude U and radiofrequency amplitude V. Stable confinement in both x and y is achieved in the overlapped region at the centre. [41]

These solutions have been obtained from [42] and for small amplitudes and a and q can be approximated as

$$u = u_1 \cos(\omega_1 t + \psi_1) + \left[\frac{q}{2}\cos(\Omega t)\right], \tag{9}$$

with $u = z, r$. The motion consists of a slow oscillation of the ion's position with frequency ω which is the secular frequency and a fast oscillation with the trap frequency called the micromotion. The secular frequency is given as.

$$\omega_i = \frac{1}{2}\Omega\sqrt{a_i + \frac{1}{2}q_i^2}. \tag{10}$$

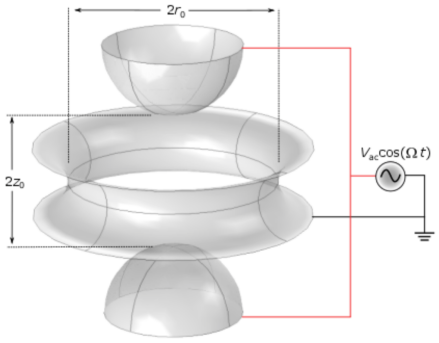

Figure 4: An ideal geometric structure of an end cap Paul trap, end caps provide a rf while the ring of radius r_0 provide rf ground [43]

2.2.1 Pseudopotential Approximation

The pseudopotential is the time averaged potential energy of an ion in a potential well, it is a useful means of describing the ion's behaviour. From which, the ion's secular frequency, trap depth and stability parameters (a, q used later to rely on to optimise our trap design) can be determined. For an oscillating electric field of $\vec{E}(r,t) = \vec{E_0}\cos(\Omega t)$, the time averaged potential experienced by the ion is

$$\widetilde{\phi} = \frac{1}{4}\frac{e|\vec{E}(r,t=0)|^2}{m\Omega^2}, \tag{11}$$

where e is the electron's charge, m is the mass of the trapped particle, Ω is the frequency of the oscillating field.

Using $\widetilde{\phi} \propto e\alpha u^2$ the secular frequency which can be found for real electrode shapes by extracting the second order coefficient α

$$\omega = \sqrt{\frac{2\alpha e}{m}}. \tag{12}$$

The above equations will be used later when simulating the behaviour of the trapping dynamics and when exploring different trap geometries.

2.3 Designing an End Cap Trap

2.3.1 Previous Designs

Prior to simulating the trapping dynamics of a new trap, the elements and design features of the previous ion trap used in [28] are examined and arguments for improvements are discussed below. Later in the thesis, a test set-up that incorporates those improvements is constructed and the initial phase of which is presented in this chapter. The cavity within the system [28] employed a robust Pound-Drever-Hall locking (PDH) scheme [44]. Despite this, a significant limitation of this system was the stability of the cavity lock. This was a great constraint on the experiment. When exploring the possible reasons, it was proposed that the entire structure of the trap, in particular the cavity-electrode assembly was insufficiently rigid.

Another key element of the cavity QED system is the mode volume of the cavity. Given that the coupling strength between the ion and cavity is proportional to the inverse of the square root of the cavity mode volume; a system in which the cavity is of minimal mode volume and within close proximity to the ion was designed. The final design used tubular electrodes with fibre cavities carefully inserted and aligned concentric with respect to the electrode. Ultrahigh vacuum compatible epoxy (LOCTITE STYCAST 2850-FT) was used to secure both components together. However, as can be seen in Fig.5 only a small quantity of epoxy was applied at the back of the electrode holding the fibre and electrode together. It has also been later found that the glass transition temperate of the epoxy was 86°C which would have altered its structural properties (to behave less like glass and more like rubber) after the bake out process, which is above this temperature. Given that the fibre diameter was 200 μm and the inner diameter was 300 μm, this left a large amount of space between the two components. Together with such a gap, the electrode length being (6 mm) and the nature of the epoxy post baking; the fibre within the assembly was unsupported and prone to vibrations. Addi-

tionally it was also recommended that a future design would feature fewer structural components.

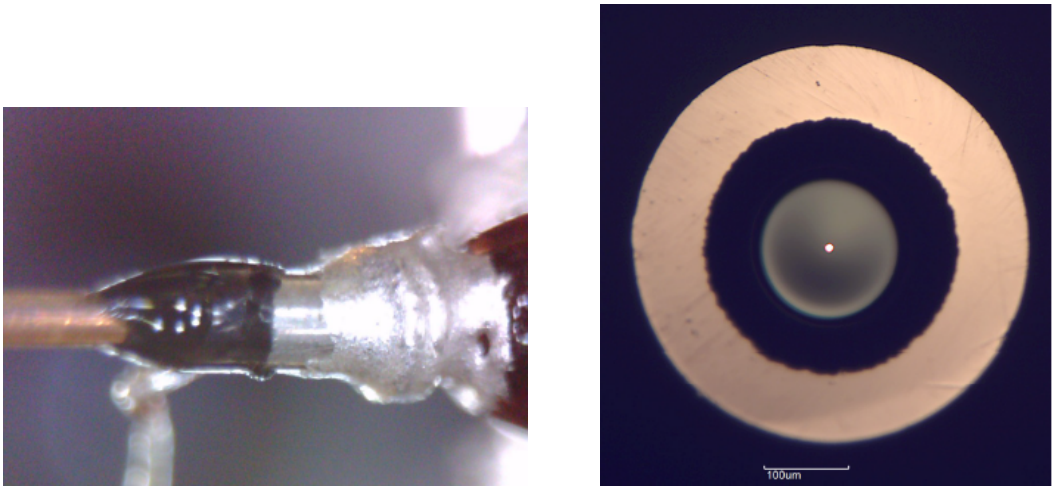

(a) (b)

Figure 5: a) Close up of the rear of electrode fibre assembly showing the quantity and location of STYCAST applied. b) Microscope image of electrode cavity assembly, highlighting the space between the fibre cavity and electrode [43].

Other limitations of the trap include optical access. The maximum angle the beams can enter the trap is 12° with the horizontal plane, this severely limits the degree to which the ion can be optically cooled. Additionally, cooling in the axial direction is also limited due to the dimensions of the trap chamber. In particular optical access through the windows was reduced due to the installation of coils to compensate for magnetised stainless steel electrodes used to provide the rf trapping field. Better cooling of the ion will allow for better localisation of the ion and hence enable larger coupling to the desired TEM_{00} mode.

In addition to limited locking stability of the cavity and poor optical access, the fibre cavity used is comprised of a single-mode (SM) fibre providing input light into the cavity and a multi-mode (MM) fibre used for florescence collection. Unlike free space cavity mirrors, which allow for the modes within the cavity to be matched with the input/output modes, fibre cavities do not have this capability. Any matching of the

modes within the cavity and the input/output light is solely the overlap of the two. Mode matching is also limited by the cavity length. When this length is greater than the Rayleigh range of the mode exiting the input SM fibre, the mode matching decreases drastically. To this end, an improved design aimed at addressing the three limitations stated above was the basis for the next design.

To address the issue of poor locking stability; the structure of the cavity-electrode assembly has been improved, this was done by changing the dimensions of the electrodes, reducing the spacing between the two from 50 μm to 10 μm. And by modifying the insertion process used in [43] a repeatable technique was developed in which both the fibre and cavity are secure as one component, this was done by filling the space between the electrode and fibre cavity with epoxy. An entirely new design increased optical access from 12°(to the horizontal) to 31°, by reducing the dimensions of the electrodes and by using gold coated copper electrodes. To increase mode matching, the new design will feature a generation of fibre cavities that incorporate integrated mode matching. This was done by concatenating a SM fibre to a Graded Index (GRIN) fibre to a MM fibre. The resulting mode matching was reported to be up to 90% for cavities of lengths up to 400 μm [45].

2.3.2 The New Design

In the system used by Takahashi et al. there exists four side electrodes which are all 1 mm away from the trap centre. Two of which provide an rf which is in phase with the main rf. This moves the pseudopotential minimum radially to optimally overlap with the cavity mode and to correct for the concentricity of the cavity inserted within the main rf electrodes. The other two side electrodes are added to provide a dc bias to allow for the compensation of micromotion. Axially, optimising the the overlap of the cavity and the ion is done by applying a dc to the main trapping electrodes. In the new design, a similar set-up is adopted in which four side electrodes are used to shift the ion's po-

sition. However, rather than repositioning the ion electronically the side electrodes are on a piezo stage and their proximity to the ion would be mechanically adjustable. By altering their relative position we aimed at perturbing the trapping potential and shifting the pseudopotential minimum; a novel approach that has not been adopted for end cap systems in other ion trapping groups. At the centre of the structure, two electrodes that provided rf with fibre cavities inserted are positioned on v-grooves. Both are on shear piezos (Noliac CASp03) that would be used to scan the cavity length over a free spectral range for the resonance position. One of the rf electrodes was adjustable with a piezo stage (TritorMini T-401-00), this was used to finely optimise cavity alignment. Surrounding the rf electrodes are the side electrodes which are connected to rf ground and are responsible for adjusting the pseudopotential minimum, these side electrodes were held by an adjustable mount controlled by a secondary stage (Tritor 100).

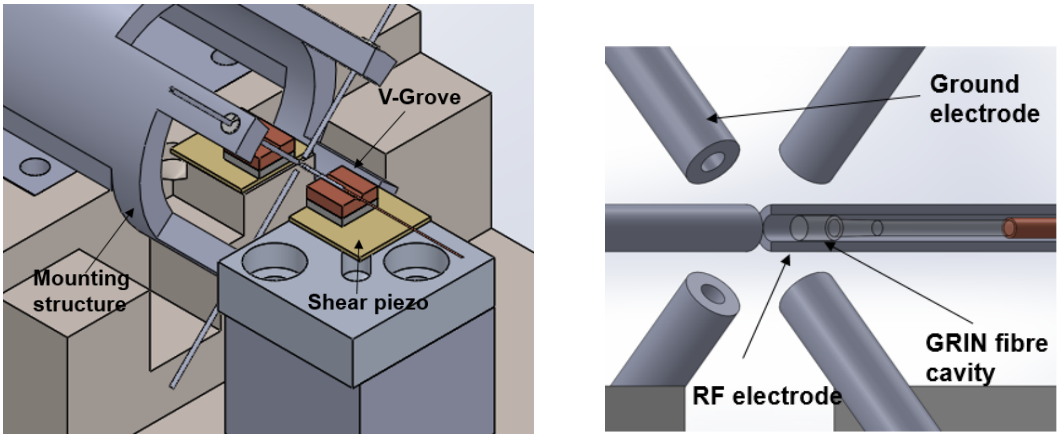

(a) (b)

Figure 6: a) Design of electrode mounting structure, showing stages and piezos used. b) A close-up view of the ion trap structure with an integrated fibre cavity. Only a cross-section of the right most electrode reveals the internal structure: fibres inside the electrodes. The side electrodes are located on the radial plane.

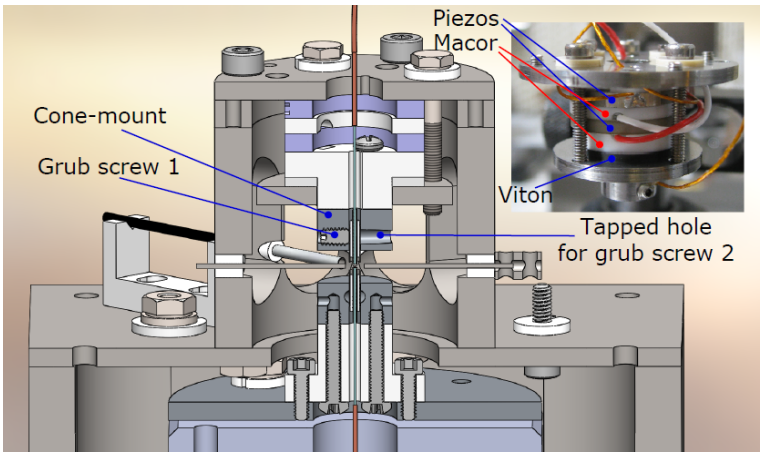

(a)

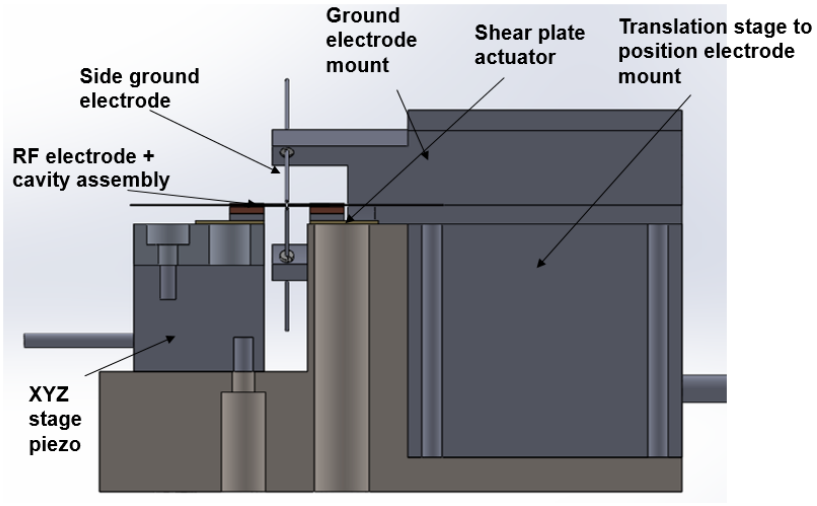

(b)

Figure 7: Cross sectional designs of the system used a) by Takahashi et al. b) a cross section of the new design.

2.3.3 Electrode Assemblies and Insertion Process

A similar procedure described in [43] was used to create our electrode-cavity assemblies is followed, however the new design features a simplified structure of a fibre inserted into a single electrode (whereas [43] uses two electrodes one inserted into the other). To preserve the finesses of the cavity, it was imperative that the cavity facet does not come into contact with the electrode inner walls during insertion. Additionally, it was aimed in creating a rigid assembly with no moving components susceptible to acoustic

vibrations within the system. To this end a process in which the space between the electrode and fibre was filled with epoxy without letting any run on the cavity face was developed. This was challenging considering that the spacing between the inner electrode wall and the cavity was only 10 μm and given the limitations of the stages, cameras and the overall set-up. Briefly; the process relied on a pre-alignment step in which the fibre and electrode were iteratively aligned to each other prior to insertion. In this setup the fibre remains fixed while the electrode is clamped to multiple rotational stages. A USB microscope camera was used to focus down the electrode and any minute variations in the concentricity of the electrode could be corrected for until the rear of the electrode and the front (insertion side) would have an optimised overlap in that respective axis as the camera is focused down the electrode. Once inserted, 80% of the fibre is retracted out of the electrode again and semi-cured epoxy is applied to this portion of the fibre. Prior to epoxy deposition, the epoxy is semi-cured to a specific duration such that it is at a viscosity that prevents capillary action from running down the fibre and contaminating the cavity facet. The fibre is reinserted again while applying minute amounts of epoxy from the back of the fibre while being reinserted.

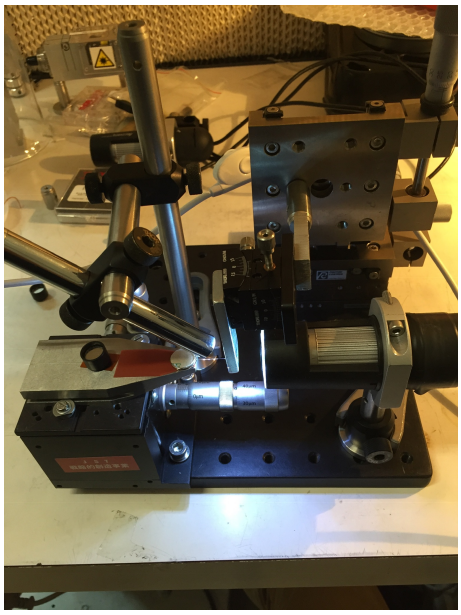

(a)

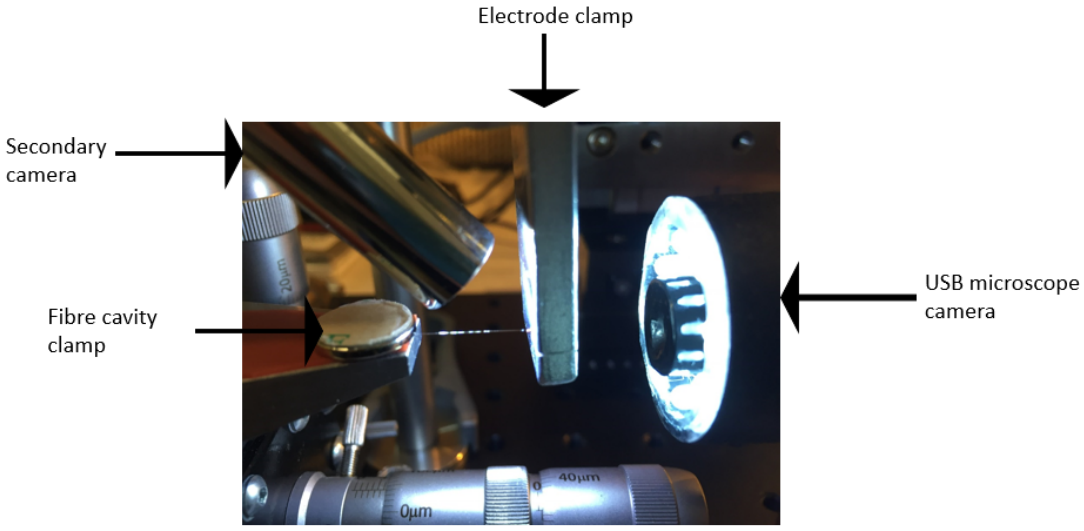

(b)

Figure 8: a) The insertion set up showing the relavant stage and cameras. b) A close up of the fibre being insertion into the electrode.

Although the final process was repeatable, achieving perfect concentricity was infeasible. Measurements of the concentricity of the fibre with respect to the electrode post alignment/insertion against post application of epoxy found that concentricity improved by approximately 50%. The reason was unknown however it was postulated that an

effect due to capillary action was the cause. Regardless, there existed some need for adjusting the pseudopotential minimum with the desired cavity mode, which will be discussed in the following subsection.

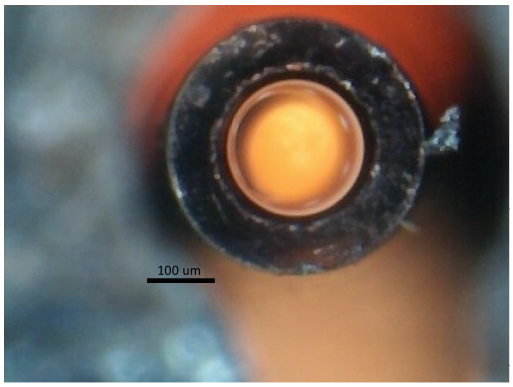

(a)

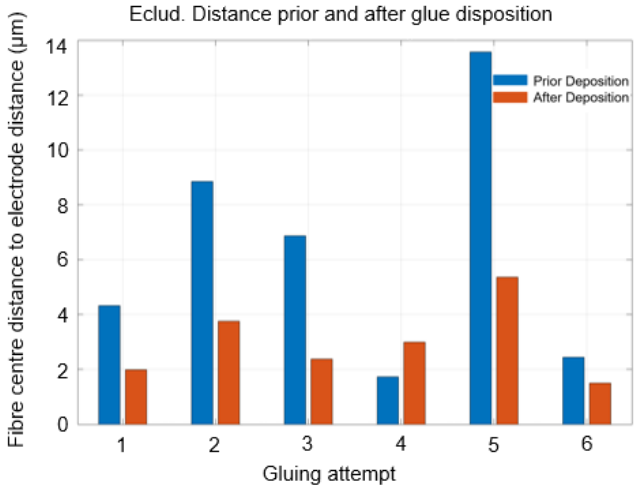

(b)

Figure 9: a) Microscope image of fibre-electrode assembly featured in the new design, this iteration features less free space between the fibre and electrode in comparison to Fig.[5]. b) The effect of epoxy deposition on the concentricity of the fibre with respect to the electrode for different insertion and gluing attempts.

As highlighted in Fig. 9b, there exists an average concentricity offset of 3 μm post expoy deposition. Attempt 5 showed an offset of 5.75 μm, hence it was anticipated that in the worst case scenario (based on the tests) the ion would need to be repositioned with respect to the cavity by 6 μm.

2.3.4 Radial Adjustment of the Ion Position

A means to adjust the position of the ion in order to maximise coupling to the cavity modes is required. As briefly described, the side electrodes are fixed with respect to one another but can be translated with respect to the trap centre. Their position can be adjusted with a piezo stage of travel of 100 μm and is controlled by adjusting the dc offset from a high voltage amplifier (Piezomechanik SVR 150/3). The four side electrodes are rf grounded and are attached to a single mounting structure. By shifting the electrodes by $+k$ the pseudopotential minima is displaced by Δx.

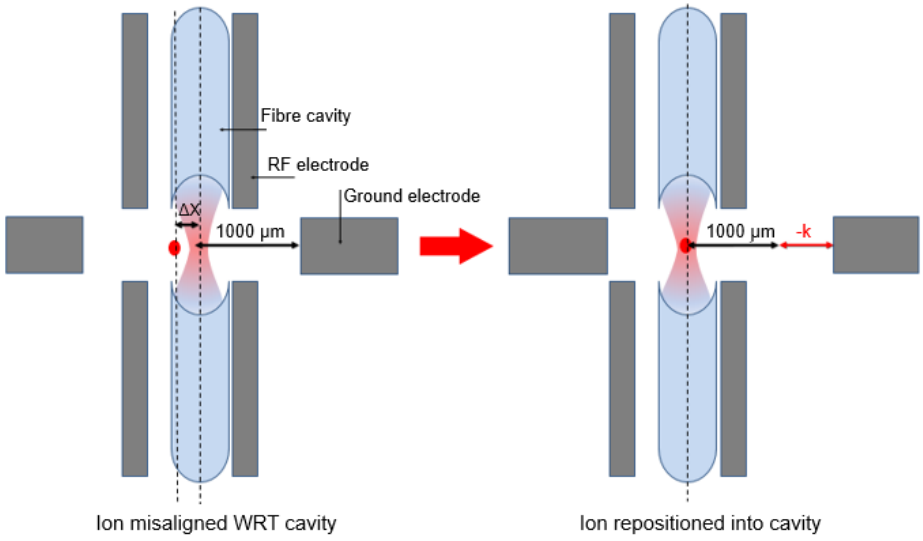

Figure 10: Schematic of fibre-electrode assembly cross section and the alignment process. For a cavity that is not concentric with respect to the electrode, repositioning the side electrodes by some distance k shifts the pseudopotential minimum by Δx to overlap with the desired mode of the cavity

From the insertion test set up it appears that a concentricity offset of 2-6 μm would have to be corrected for. In order to find the required eletrode distance to obtain a specific shift of the potential minimum, we simulate the pesudopotentials of the system. To this end a finite element simulation model to evaluate this was employed.

2.4 Simulation

As an alternate means of positioning the ion has been proposed, it is important that the geometries and mode of operation of this new trap is simulated prior to any further development of the trap. To simulate the effect of the side electrodes on the pseudopotential, a static simulation was used. The electrostatics module in COMSOL Multiphysics was employed on a geometry that replicates the structure as close as possible. A parabola was then fitted to the simulation output and the position of the minimum was obtained to determine the secular frequency of the ion. A trap drive frequency of 20 MHz and an rf voltage of 200 V were used to calculate the pseudopotential (9). In the simulation the axial direction was taken to lie along the cavity. About the trap centre it was observed that the potential minimum does not maintain spherical symmetry, this is due to the nature of the trapping geometry and the proximity of the electrodes.

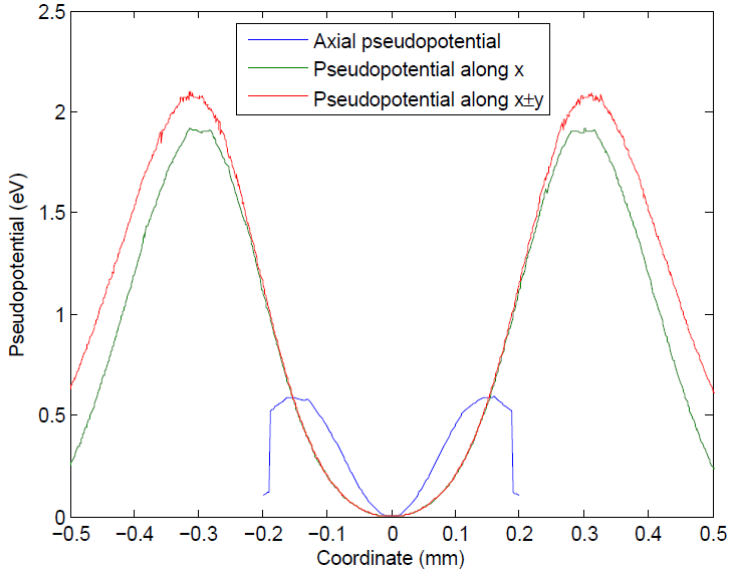

Figure 11: Simulated potential in both axial and radial directions. We observe different shapes due to the presence of geometric asymmetries. Axially the presence of the fibre-electrode assembly causes the tailing off of the potential at ± 200 μm [43]

2.4.1 Results

To determine how much the potential minimum will shift due to our displaced side electrodes, multiple simulations with varying the positions of the side electrodes were carried out. By default the side electrodes were of a distance of 1 mm from the trap centre. It was observed that the closer the side electrodes were to the trap centre; the less travel was required to shift the potential minimum, however this would compromise optical access.

Given that the Tritor 100 is limited to a travel of 100 μm and by extrapolating the lines in Fig. 9 it can be approximated that to correct for the potential offset in concentricity found in 2.3.3, while maximising optical access, the side electrodes would be positioned at a distance of (750 - 1000) μm from the trap centre.

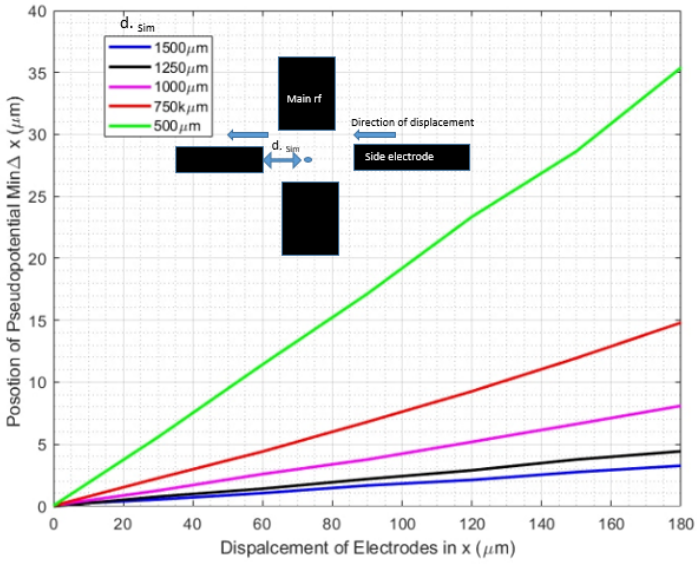

d_{Sim} (μm)	gradient
1500	0.010
1250	0.016
1000	0.050
750	0.092
500	0.200

Figure 12: left: Position of potential minimum for different electrode-ion separations, a linear relation is preserved as the side electrodes are moved closer/further to the trap centre. Right: table of gradients for the multiple slopes of the position of the pseudopotential min with different electrode-ion separations (d.sim).

By taking into account both the degree to which the potential minimum would need to be shifted and the optimal optical access that can be obtained. An optical access angle of 28° and 31° to the vertical and a horizontal plane respectively was measured. By

following the analysis in 2.2.1 in which a parabolic line shape is fitted to the potential, the secular frequency of the ion as the potential minimum is perturbed can be extracted. Driven at a frequency of 20 MHz the secular frequencies for a ion of mass ^{40}Ca remain within reasonable values of 2 MHz with a variation of only 100 kHz as the side electrodes are shifted.

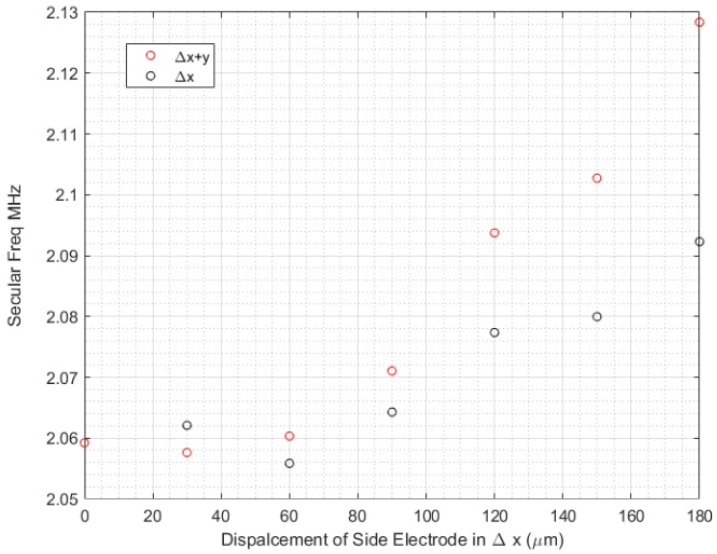

Figure 13: Secular frequencies for the ion when side electrodes are shifted in x and x+y

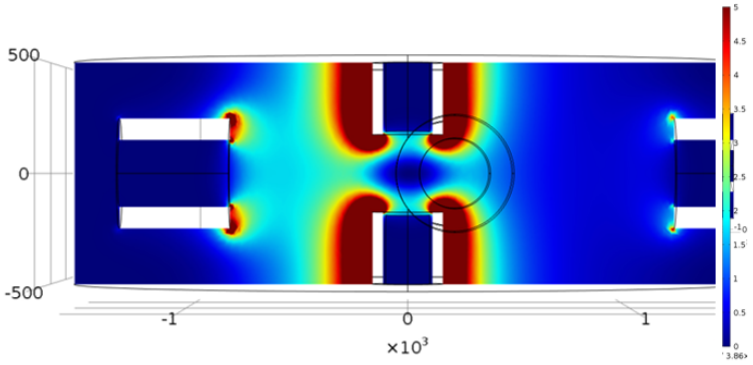

Figure 14: Pseudopotential in eV of the trap cross section when the side electrodes are displaced by 100 μm.

From the simulations it can be concluded that it is feasible to move the ion's position to the cavity centre given the travel of the piezo while maintaining good optical access. From this, the side electrodes will be placed 1 mm from the trap centre. Despite the

effect of distorting the potential with the side electrodes it can be observed that the secular frequencies do not vary by much and remain within reasonable values. However before constructing the new trap a test is required to assess the cavity's ability to remain locked on resonance with the proposed main rf electrode structure. In the following section a test set-up is built based on the electrode fibre assembly design that has been tested in the insertions step Fig.8.

3 Implementing Fibre Cavities for cQED

3.1 Introduction

Thus far a number of improvements for the new trap have been proposed and a preliminary trapping simulation suggests that such are feasible. In this chapter, our attention is now brought to the optical elements of the system by implementing fibre cavities into our set-up. Optical cavities, namely the Fabry Perot cavity has been a major component in the development of lasers, interferometers and parametric oscillators. A cavity with a high finesse will have a lower photon decay rate (κ) and hence it is desirable to have high finesse cavities in reaching the strong coupling regime. In recent years the development of high quality optical cavities machined on the end facets of fibres have been a promising route towards miniaturising such systems. They have proven successful in achieving strong coupling with an ensemble of neutral atoms and single ions [28],[46]. The following discussion begins by highlighting why fibre cavities are a promising route towards strongly coupled cQED experiments; in particular how their size leads to this. The approach used in this thesis uncovers a number of issues associated with their implementation, the discussion that follows highlights their potential drawbacks. This is elucidated by attempting to set up a robust Pound-Drever-Hall (PDH) locking scheme. As an overview of this chapter; some theory on Fabry Perot cavities are initially presented which will be used later when discussing the PDH set-up and will end by examining the system's inability to effectively lock on resonance.

3.2 Optical Cavities

Prior to any discussions, a basic understanding on the theoretical framework of optical cavities is required. The reflectivity coefficient is derived which is required in understanding how an error signal is generated in the PDH scheme. How the quality of

an optical cavity is characterised is briefly discussed, followed by a brief overview of impedance matching.

Reflection Coefficient

Beginning with the simplest case of two mirrors with their degree of reflection and transmission defined by the constants r and t respectively. On the assumption that there are no losses due to absorption or scattering the following holds; $r^2 + t^2 = 1$ ($r_1 = r_2$). The incoming light of frequency ω, amplitude E_0 is described by

$$E_i = E_0 e^{i(k_x \cdot x - \omega t)}. \tag{13}$$

Once light has entered the cavity, a portion is immediately reflected (E_r) and undergoes a π phase shift. The promptly reflected beam is expressed as

$$E_{r1} = E_i r e^{i\pi}. \tag{14}$$

This light does not enter the cavity and hence does not undergo any circulation. The

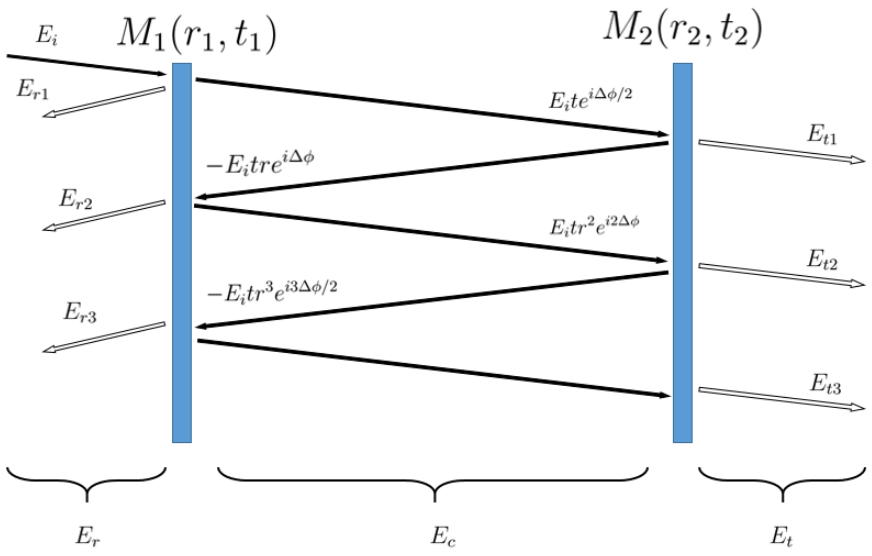

Figure 15: The basic scheme of a Fabry Perot optical cavity, two mirrors with corresponding reflection and transmissions(r,t). Some light is 'leaked' out of the cavity from both the input and output sides, the sum of which form E_r or E_t. Within the cavity we observe how the build up of the circulating light (E_c) is formed.

additional reflected beams are the result of circulation within the cavity and incur a phase shift of $\Delta\phi$ (2π).

$$E_{r2} = E_i t^2 r e^{i\Delta\phi} \tag{15}$$

$$E_{r3} = E_i t^2 r^3 e^{i2\Delta\phi}. \tag{16}$$

The reflected beams can be generalised for all but $n = 1$, in the following expression

$$E_{rn} = E_i t^2 r^{2n-3} e^{i(2n-2)\frac{\Delta\phi}{2}}. \tag{17}$$

The total reflected light is the sum over all round trips

$$E_r = -rE_i + E_i t^2 r e^{i\Delta\phi} \sum_{j=2}^{n} (r^2 e^{i\Delta\phi})^{j-2}. \tag{18}$$

Using the geometric series the sum can be expressed as

$$E_r = -E_i r + E_i t^2 r e^{i\Delta\phi} \frac{1}{1 - r^2 e^{i\Delta\phi}}. \tag{19}$$

The ratio of the reflected field to the incident field gives us the reflection coefficient of the cavity

$$\mathcal{R} = \frac{E_r}{E_i} = \frac{r(e^{i\Delta\phi} - 1)}{1 - r^2 e^{i\Delta\phi}}. \tag{20}$$

The reflected field comprises of the promptly reflected beam that does not enter the cavity and the circulating beam that leaks from the cavity on the side of mirror 1 (M_1). This term will be returned to later when analysing the nature of the reflected field, in particular when modulating the input beam. Following a similar analysis the expression for the transmission coefficient is stated [47].

$$\mathcal{T} = \frac{1}{1 + \frac{4r}{(1-r)^2}\sin^2(i\frac{\Delta\phi}{2})}. \tag{21}$$

For a system in which $I_t \to 1$, the cavity is said to be on resonance. This occurs when the length of the cavity is an integer multiple of half wavelengths, i.e. when the light circulating in the cavity is in phase during each round trip. However a cavity's ability to be a resonator rests upon the mirror's reflectivity. Typically optical cavities are characterised by their finesse ($\mathcal{F}$). Finesse can be thought of as the number of times a photon circulates a cavity before it decays, and can be expressed as

$$\mathcal{F} = \frac{\pi\sqrt{r}}{1-r}. \tag{22}$$

The case of $r = 1$ means that light undergoes no losses upon reflection, in reality $r < 1$ and the amplitude will always reduce for every round trip. Measurement of the reflectivity can be particularly cumbersome, hence a finesse measurement can be done by taking the ratio of the linewidth of the resonance peaks ($\Delta\phi_{FMWH}$) in transmission with the frequency difference between two successful reflected/transmitted intensity maxima; known as the free spectral range (ν_{FSR}). Defined as the frequency difference between two successive reflected/transmitted intensity maxima.

$$\mathcal{F} = \frac{\nu_{FSR}}{\Delta\phi_{FWHM}}. \tag{23}$$

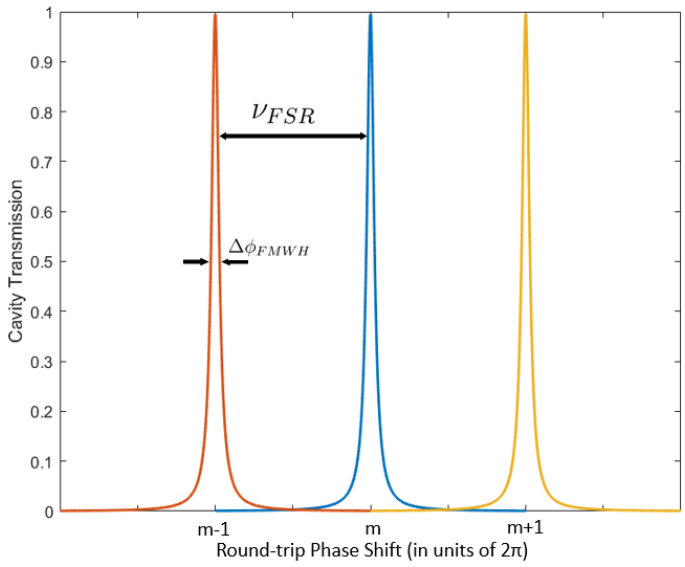

Figure 16: Cavity transmission for a lossless system showing three transmission peaks spaced a FSR apart.

Impedance Matching

Thus far a lossless system in which $\mathcal{L} + \mathcal{T} = 1$ (for some loss coefficient $\mathcal{L}$) and the reflectivity of both mirrors are equal has been assumed, however very typically mirrors that do not meet this criteria are often the case. On resonance, it is expected that destructive interference in the reflected wave is observed; this is signalled as a dip in the reflected light's intensity. For two mirrors of different reflection and transmission coefficients (r_1, t_1, r_2, t_2), the change due to a round trip is defined as

$$\tilde{g}_{r,t} = r_1 r_2 e^{2\Delta\phi}. \tag{24}$$

The field circulating within the cavity is stated as

$$E_{cir} = E_i \frac{t_1}{1 - \tilde{g}_{r,t}}. \tag{25}$$

Using $\tilde{g}_{r,t}$ the expression for the reflected field can be rewritten as

$$E_r = r_1 E_i - \frac{E_i t_1^2 \tilde{g}_{r,t}}{r_1 \tilde{g}_{r,t}}, \tag{26}$$

and the transmitted field as

$$E_t = -t_1 t_2 \frac{E - ie^{i\Delta\phi/2}}{1 - \tilde{g}_{r,t}}. \tag{27}$$

For a cavity that satisfies the resonance condition ($d/\lambda = n/2$), we can see that $e^{\frac{2\pi d}{\lambda}} = 1$ (for n being some integer) and for the case when $r_1 = r_2$; on resonance

$$\frac{E_c}{E_i} = \frac{t}{1 - r^2}. \tag{28}$$

Given that $t^2 + r^2 = 1$, therefore

$$\frac{E_c}{E_i} = \frac{1}{t}. \tag{29}$$

The intensity ($|E|^2 \propto I$) of the circulating light per input intensity is given by

$$\frac{I_c}{I_i} = \frac{1}{1 - r^2}. \tag{30}$$

For the case where the cavity is on resonance and the reflectivity are the same for both mirrors (impedance matched) is $r^2 = 0.999$, $I_i = 1$ mW and $I_c = 100$ mW. Similarity the intensity of the reflected light $I_r/I_i = 0$W, this would correspond to a drop in intensity about the resonance position. However for the case when the same input power of 1 mW into cavity the but the cavity is not impedance matched ($r_1 \neq r_2$), e.g. $r_1 = 0.99$ and $r_2 = 0.995$, a similar analysis would yield a circulating power of 89 mW and a transmitted and reflected power of 0.888 W and 0.112 W respectively. An impedance matched cavity is not required for our set-up, however a good degree of impedance matching is useful in generating a PDH error signal. Knowing that at resonance the reflected beam would be of minimum intensity. The PDH error signal would ideally be generated from the reflected light from the cavity. This was proven problematic as shall be observed later.

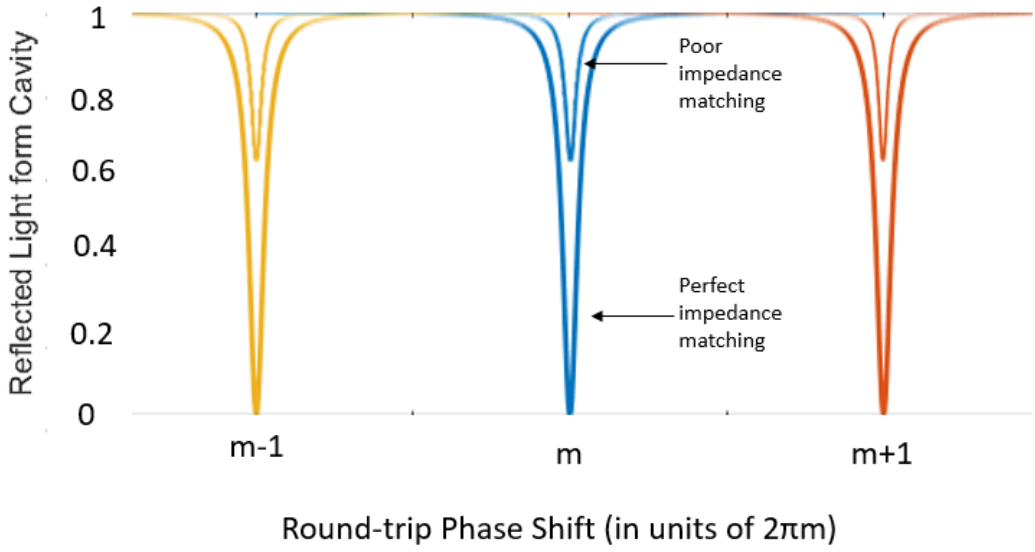

Figure 17: Destructive interference at resonance causes dips in the reflected signal, a perfectly impedance matched cavity with mirrors of matched reflectivity will exhibit complete destructive interference; no light is reflected on resonance, a less impedance matched cavity will exhibit less interference.

The Fundamental Mode

The light resonant with the cavity is typically of the Gauss-Hermite form. Spatially the light within the cavity is comprised of longitudinal and transverse mode functions of the form

$$E_{lm}(x,y,z) = E_0\Phi(x,y,z)\Psi_l(x,z)\Psi_m(y,z), \tag{31}$$

where Φ describes the longitudinal modes and the transverse modes are described by $\Psi_{l,m}$. The transverse modes are described by Hermite Polynomials H_l & H_m which describe a form of the radial field distribution. Each form is described as a transverse mode of the EM field (TEM_{lm}). The transverse mode structure is given by

$$\Psi_{lm}(x,y,z) = \sqrt{\frac{\omega_0}{\omega(z)}} H_{lm}\frac{\sqrt{2}(x,y)}{\omega(z)} e^{(-x^2+y^2)/\omega^2}, \tag{32}$$

for $\omega(z)$ is the mode radius along z, z_R is the Rayleigh range

$$\omega(z) = \omega_0 \sqrt{1 + \left(\frac{z}{z_R}\right)^2}. \tag{33}$$

The fundamental mode (TEM_{00}) has a Gaussian profile and has the smallest mode volume for the cavity mirrors used.

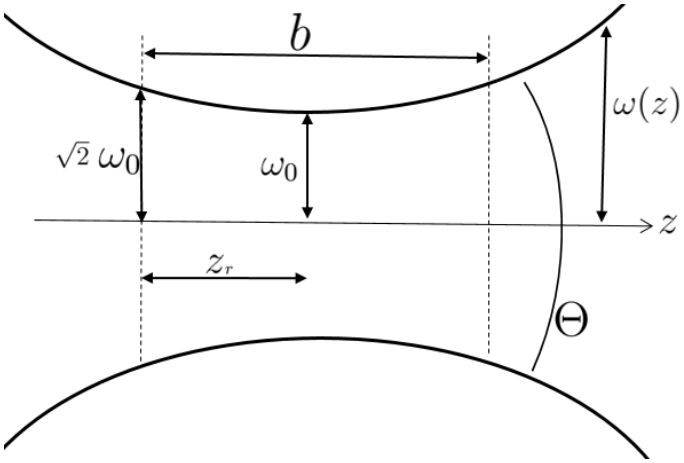

Figure 18: Profile of the fundamental mode/Gaussian (TEM_{00})beam showing the mode waist (ω_0), Rayleigh range ($z_R = \pi\omega^2/\lambda$) for a beam propagating along the axial (z) direction. For $z \gg z_R$, $\omega(z)$ increases linearly with z.

The Rayleigh range ($z_r = \frac{\pi\omega_0^2}{\lambda}$) is defined as the distance from the centre of the beam waist (in the direction of propagation) where the beam radius increases by a factor of $\sqrt{2}$. The spatial wave function/distribution for the fundamental mode is described as

$$\Psi_{00}(x, y) = \frac{\omega_0}{\omega(z)} e^{(-x^2+y^2)/\omega^2}. \tag{34}$$

For a given frequency the cavity supports (which is determined by the reflective coating), the mode waist is limited by the cavity's boundary conditions namely R_{oci}. A useful parameter is the resonator g parameter, as defined in [48] as $g = 1 - L/R_{oci}$ for each mirror.

$$\omega_0^2 = \frac{L_0\lambda}{\pi}\sqrt{\frac{g_1 g_2(1-g_1 g_2)}{(g_1+g_2-2g_1 g_2)^2}}, \tag{35}$$

in which a stable region exists in the range $0 \leq g_1 g_2 \leq 1$. This requirement is one that is to be met for the presence of a low-loss standing wave in the cavity. Cavity mirrors can be comprised of different mirror shapes. Symmetric cavities in which $R_1 = R_2$, plane parallel ($R_1 = R_2 = \infty$), symmetric confocal cavities ($R_1 = R_2 = L$), symmetric concentric ($R_1 + R_2 = L$) are some examples.

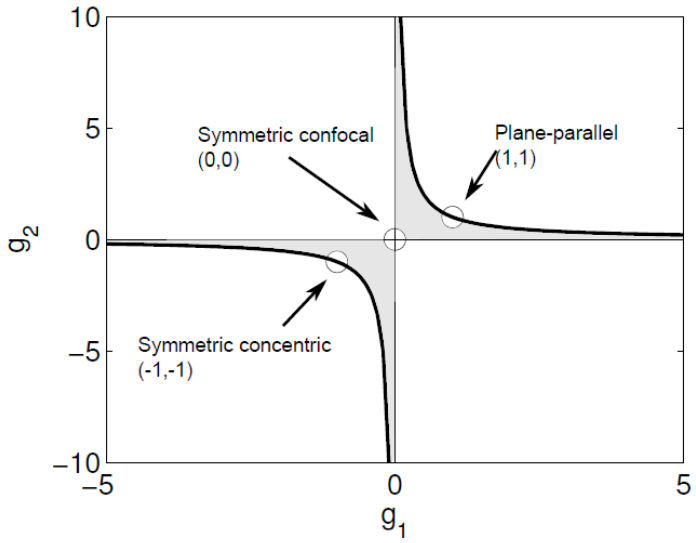

Figure 19: The cavity stability showing stable regions in grey and their corresponding cavity shapes for different values of g_1 and g_2. [41]

As mentioned previously, the fundamental mode features the smallest mode volume for our cavities. This minimal mode volume increases the coupling strength of our ion to the cavity and reduces the amount of losses due to clipping or diffraction losses. These losses reduce the finesse of our cavity and can be addressed by optimal cavity alignment and mode matching. The matching of modes is typically done with mode matching optics in which the profile of the injected mode matches that of the cavity mode. However, as the cavities used in our set-up are fibre based, the issue of matching the modes of the incoming light in the input fibre and the cavity are of particular relevance as the

input mode is fixed and given by the fibre output. A theoretical breakdown of the mode matching problem comparing fibre based cavities and free space cavities are presented in [46].

3.3 Benefits of Fibre Cavities

Thus far, the theory and background of fibre cavities have been introduced without an explanation as to why they are desirable in our cQED system. In the context of cQED with ions; a desirable resonator is one that maximises the coupling between the quantum emitter (in this case a trapped ion) and the optical modes, this can be enhanced by optimising a number of parameters. For example, the relative alignment of both mirrors to yield the desired mode and selecting cavity mirrors that yield the smallest mode volume both maximise coupling. Atom-cavity coupling is often quantified through cooperativity ($C \propto g^2/2\kappa\gamma$), said quantity takes the ratio of the coupling strength g, and the decay rate of both the cavity and the atomic decay rate κ, γ respectively. The coupling strength scales with the mode volume as $C \propto \mathcal{F}/\omega_0$, it is thus desirable to have high finesse cavities with minimal mode volume. To this end, fibre based fabry perot cavities have been successful in achieving optimal coupling with a single ion. The fibre cavities in this study featured a radius of curvature in the range of $(400-700)\,\mu$m, cavity length of L $\sim 400\,\mu$m and finesse of $\mathcal{F} \sim 50,000$ and exhibited low birefringence. Free-space bulk cavities allow the matching of modes within the cavity with external mode-matching optics. Typically this is done with a lens with some focal length (f) placed at an adjustable distance. A similar architecture for fibre based cavities has been developed in which a graded-index fibre (GRIN OFS, BF04432-1) with a specific gradient constant, allows us to determine the focal length used.

The result of a careful process of cleaving and splicing yields a concatenated SM, GRIN and MM fibre assembly. These fibre cavities hence feature integrated mode matching optics [45] of a mode matching efficiency of up to 90%, where as standard fibre cavities

feature a mode matching efficiently of up to 30%, said assembled fibres will be referred to as GRIN fibre assemblies.

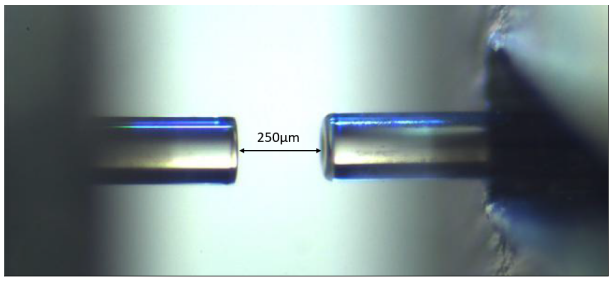

(a)

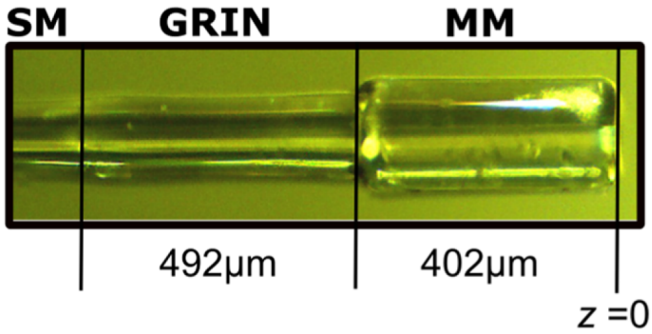

(b)

Figure 20: a) A fibre based cavity of cavity length 250μm, [43]b) A GRIN fibre assembly showing the concatenated structure of the SM+GRIN+MM fibres and their respective lengths [45].

The procedure to fabricate the mirror and shape on the end facet of the MM fibre is one that is repeatable and reliable [49]. A CO_2 laser shoots the end facet of the fibre to create a curved surface. The profile of curvature is deduced with a Michelson interferometer and a Guassian fit allows us to determine the radius of curvature. The shot facets are stored and handled carefully to avoid contamination and then sent to be coated (Advanced Thin Films-Boulder, Colorado USA) with a high reflective coating that is specific to our desired wavelength (866 nm).

Given that fibre optics are the preferred means of channelling photons over long distance with minimal decoherence [50], the inherent fibre coupling that exists with fibre based cavities leads to the prevalence of fewer losses when the output of the cavity is the fibre.

3.4 Developing a Stable Fibre Cavity System

As stated in previous sections a limitation of the trap used in [28] was its inability to remain locked on resonance in the presence of acoustic noise. In this subchapter, the theory of PDH locking is presented which will use some of the results of the derivation presented in Section 3.2 as well as presenting our experimental apparatus. As stated previously the cavity transmission intensity is frequency specific. The resonance condition is one that is set by a specific cavity length and a means to maintain this strict condition is the motivation for this section. Here the Pound-Drever Hall technique is introduced and the implementation is discussed. A number of issues in the system are uncovered and this leads to a discussion of the less obvious drawbacks associated with fibre based cavities which will be presented in the following subsection.

3.4.1 Pound-Drever-Hall Locking Scheme

Modern implementations of the Pound-Drever Hall (PDH) method are able to deliver sub-Hz stability [51]. Typically used to stabilise the frequency of a laser to a stable cavity, in some cases the reverse is implemented in which a stable laser is used to lock an unstable cavity at its resonance position. In the former a signal is fed to a servo amplifier which in turn modifies the laser frequency to minimise some error. In the latter, a feedback loop sends a signal to an actuator that modifies the cavity length away from any spatial deviations.

Fig. 16 shows how the intensity of the promptly reflected signal varies as a function of round trip phase, which is dependent on the cavity length. It can be seen that minute changes about the resonance position will induce large changes in the reflected (or transmitted) intensity. These change as a function of cavity length (or input frequency) are independent on the input laser intensity. One could set up a scheme that locks to this signal, however, as the reflection intensity is symmetric about resonance; the system would have no means of differentiating between which side of the resonance position

the cavity is on.

Conversely, the derivative of the reflection coefficient (eq.20) with respect to the cavity's position, is antisymmetric about resonance. This is because of the phase difference above and below resonance. However, as phase alone is not a directly measurable property, the PDH method allows us to indirectly measure this disparity via an optical measurement. This is done by modulating the input beam using an electro-optical modulator and taking the phase relation of the carrier and sidebands. The basic setup is shown in Fig.23.

Quantitative Model

Our input field with the absence of modulation is simply (13), $E_i = E_0 e^{i\omega t}$. We rewrite the reflection coefficient in terms of ω as

$$\mathcal{R}(\omega) = \frac{E_r}{E_i} = \frac{r\left(e^{i\frac{\omega}{\Delta\nu_{FSR}}} - 1\right)}{1 - r^2 e^{i\frac{\omega}{\Delta\nu_{FSR}}}}. \tag{36}$$

To highlight the phase relation we treat our input light with a constant frequency, the reflected beam is comprised of the light that is immediately reflected from the input side and the light that exits the cavity due to the build up between the two mirrors. On resonance the two beams interfere destructively which correspond to the dips we observe in Fig. 16. When the cavity length is slightly off the resonance condition but such that there exists a build up of light, the phase relation difference between the two beams is not π and does not undergo complete destructive interfere.

An input beam (of frequency ω) is phase modulated at a frequency of Ω has the form

$$E_{in} = E_0 e^{i(\omega t + \beta \sin(\Omega) t)}, \tag{37}$$

$\beta \sin(\Omega)t$ is the phase incurred due to the modulation. Using Bessel functions ($J_0(\beta)$, $J_1(\beta)$) we can express (37) as

$$E_{in} \approx E_0[J_0(\beta)e^{i\omega t} + J_1(\beta)e^{i(\omega+\Omega)t} - J_1(\beta)e^{i(\omega-\Omega)t}], \tag{38}$$

where the first term in the square parenthesis is our carrier and the second and third term correspond to the sidebands. The total input power is give by $P_0 = \mid E_0 \mid^2$ and hence $P_c = J_0^2(\beta)P_0$ and $P_s = J_1^2(\beta)P_0$ are the powers in the carrier and sidebands respectively. When the modulation depth (amplitude) is low, the assumption that all power is in the carrier and first order sidebands holds. Namely that $P_0 \approx 2P_s + P_c$. The reflected light is expressed as

$$E_{ref} = E_0[F(\omega)J_0(\beta)e^{i\omega t} + F(\omega+\Omega)J_1(\beta)e^{i(\omega+\Omega)t} - F(\omega-\Omega)J_1(\beta)e^{i}\omega - \Omega t]. \tag{39}$$

Following the notation used in [44] the reflection coefficient ($\mathcal{R}(\omega)$) is expressed as F(ω). The quantity that is measured, is the power on the photodetector, which is

$$\begin{aligned} P \propto \mid E_{ref} \mid = P_c \mid F(\omega) \mid^2 + P_s F \mid (\omega+\Omega) \mid^2 + \mid F(\omega-\Omega) \mid^2 + \\ \sqrt{P_c P_s} Re[F(\omega)F^*(\omega+\Omega) - F^*(\omega)F(\omega-\Omega)] \cos(\Omega t) \\ + ImF(\omega)F^*(\omega+\Omega) - F^*(\omega)F(\omega-\Omega)] \sin(\Omega t) + (2\Omega \text{ terms}). \end{aligned} \tag{40}$$

We are interested in the two terms oscillating at a modulation frequency of Ω as it contains information of the phase of the reflected signal. We are interested in terms

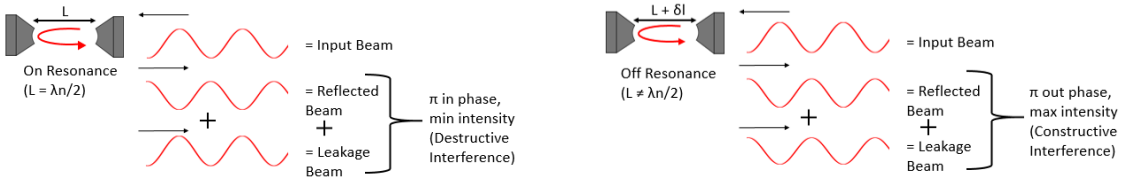

(a) (b)

Figure 21: a) A schematic of the phase difference incurred in the reflected beam when the cavity is a) on resonance and b) off resonance

containing

$$F(\omega)F^*(\omega+\Omega) - F^*(\omega)F(\omega-\Omega). \tag{41}$$

Hence the terms that oscillate with $\sin(\omega t)$ and $\cos(\omega t)$. A device known as a mixer combines the signal used to modulate the input beam with the light reflected from the cavity of the same frequency. It isolates all but the oscillating terms by taking the product of the two inputs. One input being from the reflected signal (P_{ref}) and the other the local oscillator (of frequency Ω'). The product of which is

$$\sin(\Omega t)\sin(\Omega' t) = \frac{1}{2}[\cos(\Omega-\Omega')t] - \cos[(\Omega+\Omega')t]. \tag{42}$$

Depending on the inputs of the mixer, the output will contain terms of both the sum $(\Omega+\Omega')$ and difference $(\Omega-\Omega')$ of the modulated signal and the signal from the local oscillator. If $\Omega=\Omega'$, our $\cos[(\Omega-\Omega')t]$ term will yield a constant (dc) signal, our error signal. But given a phase difference of $\pi/2$ between the two signals we get

$$\sin(\Omega t)\cos(\Omega' t) = \frac{1}{2}[\sin[(\Omega-\Omega')t] - \sin[(\Omega+\Omega' t)]. \tag{43}$$

For $\Omega=\Omega'$, our dc signal vanishes. Therefore to successfully generate our error signal we need to adjust the phase between the two signals accordingly [44].

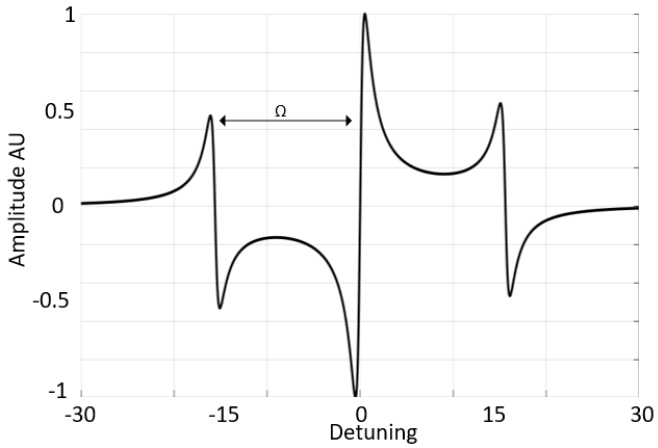

Figure 22: A PDH error signal generated with the reflected light, this error signal was generated for an optimised phase, maxium amplitude is given by $2\sqrt{P_c P_s}$, the sideband separation corresponds to the modulation frequency Ω.

Given that the cavity is fibre based, to minimise losses the majority of the beams are fibre coupled. An input beam of 866 nm is locked to a wavelength meter and shows the input beam fibre coupled to a polarisation maintaining (PM) SM-fibre. The beam is phase modulated with a fibre based EOM at a modulation frequency of 190 MHz. Light enters the cavity and a fibre based beam splitter is used to split the reflected beam which is comprised of the circulating light and the beam that is promptly reflected from the surface of the input mirror. The split beam enters a fast photo detector (FPD) that sends the signal to a mixer (Mini circuits Mixer ZAY-3) that combines the signal used to modulate the input beam with the reflected light from the cavity of the same frequency. The product of the two signals varies for different sides on resonance. This output is our measure of error on the cavity length, it is referred to as the the error signal and denoted ϵ. The entire setup works to minimise this error to zero. The desired part of the mixed signal is isolated with a low pass filter (LPF) and a feedback circuit comprised of a proportional and integral circuit generates a signal that is amplified with a piezo driver (PiezoDrive HVA PDm200)/high voltage amplifier (HVA). This is then sent to an actuator that corrects the cavity length. In the following subsection, the PDH scheme is tested and by doing so a number of issues were uncovered, a few of

which elucidate the lesser known drawbacks of fibre cavities.

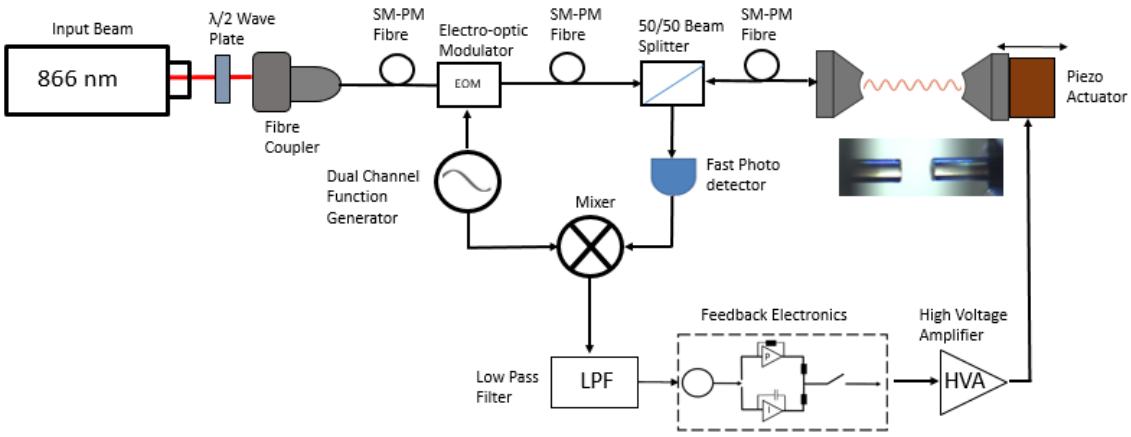

Figure 23: A schematic of a PDH system. The 866nm is locked to a wavelength meter. The $\lambda/2$ wave plate is used to shift the polarisation direction of linearly polarised light. All fibres (beam splitter included) are single mode (SM) polarisation maintaining (PM).

3.5 Drawbacks of Fibre Cavities

Although fibre cavities come with many benefits, there are also a number of drawbacks associated with their implementation. A particular issue that has been reported is the non-spherical laser-ablations which can lead to polarisation-mode splitting [46]. Another issue which was of particular relevance to our set up was the inherent in-fibre coupling of the fibre cavity mode which is greatly limited by the alignment of the cavity. Arguably our greatest challenge was engineering a rigid structure (not susceptible to vibrations) while maximising optical access and maintaining some means of in situ alignment. These issues became apparent while attempting to generate an error signal in reflection and in locking the fibre cavity to an error signal in transmission. This was uncovered during the attempt to test the new electrode-fibre assembly outlined in chapter 2.3. The aim of the test setup was in assessing the locking stability with the improved insertion process outlined in Chapter 2.

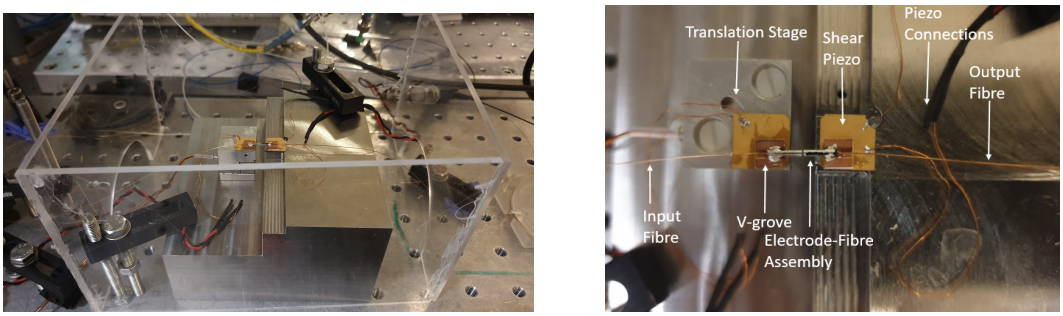

(a) (b)

Figure 24: a) The test set up showing the mounting structure and relevant electrical and optical connections enclosed in a protective perspex housing. b) A close up on the two electrode-cavity assemblies

3.5.1 The Setup

The setup in outlined in Fig.23, to best replicate the proposed trap design in chapter 2. The test setup is a simplified version of the final design presented in Chapter 2 and comprises of a mount in which the output of the cavity is fixed and a 3D translation stage (TritorMini, T-401-00) with a travel of 38 μm. The electrode-fibre assemblies are fixed onto v-groves with a conductive epoxy and are carefully aligned with respect to each other with translation stages. Once the cavities are coarsely aligned at a length of $\sim$ 200 μm they are glued with UHV compatible epoxy (EpoxyTek H21D) onto shear piezos (Noliac Piezo CSAp03) with a free stroke of 1.5 μm.

Once the epoxy cures, the Tritor stage allows for fine cavity alignment. A finesse of 23,000 was measured, however over time as the setup was continuously modified and the protective housing open, a reduction in finesse to 14,000 was observed.

3.5.2 Generating an Error Signal in Transmission

The initial test was to observe an error signal in reflection. However, despite adjusting the relative phase of the local oscillator and the modulation frequency a slow oscillation in offset in the reflected beam was observed. This variation was of $\sim$ 5 Hz. It was concluded that variations in the interference of the reflected beam was the cause.

Given that the EOM is polarisation dependant and despite using polarisation maintaining (PM) fibres, our fibre cavity is a SM non-polarisation maintaining fibre. It was likely that oscillations in the polarisation of the reflected beam was causing this. It was later found that upon generating the error signal used in [43], the authors also encountered the same issue. Unless a PM fibre was used as the cavity fibre, polarisation will constantly vary.

A solution would be to generate an error signal in transmission. However, this would be limited by the response time of the cavity. Any cavity fluctuations that occur on a time scale greater than the circulating time cannot be detected in an error signal in transmission and hence cannot be corrected for. Under arbitrary parameters, the amplitude of our error signal was 60 mV_{pp}. By adjusting the phase of the local oscillator and the modulation frequency, it was found that the optimal frequency was about the linewidth (45 MHz). Further optimisation lead to an increase in amplitude of the error signal in transmission by a factor of 10 (600 mV_{pp})

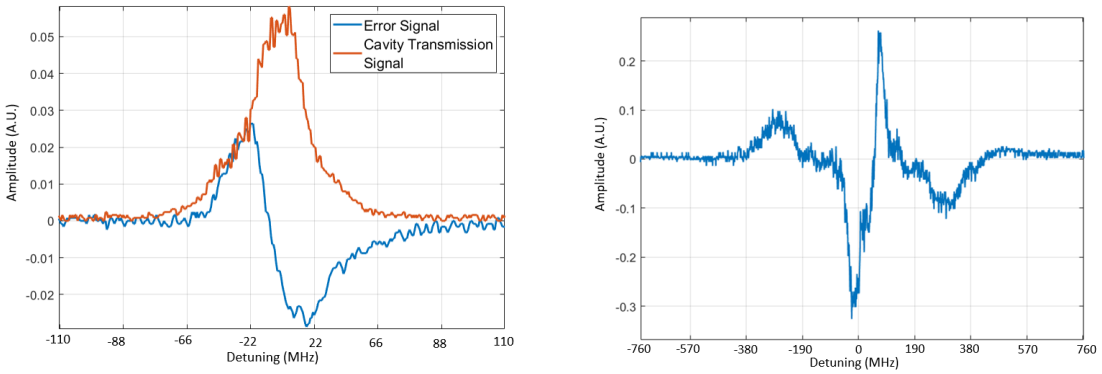

(a) (b)

Figure 25: a) Cavity transmission of linewidth at half maximum of 45 MHz. The generated error signal is for an arbitrary set of parameters. b) The error signal for an optimised modulation frequency of $\Omega = 45$ MHz.

As it is desirable to maximise the amplitude of the error signal, the PDH error signal for an impedance matched ($r_1 = r_2$) cavity of FSR = 3.1 MHz and FWHM = 1.9 GHz was simulated. The modulation frequency for a range of $0 - 5(\Delta\phi_{FWHM})$ was varied

and their lineshapes plotted along with their amplitudes as a function of Ω.

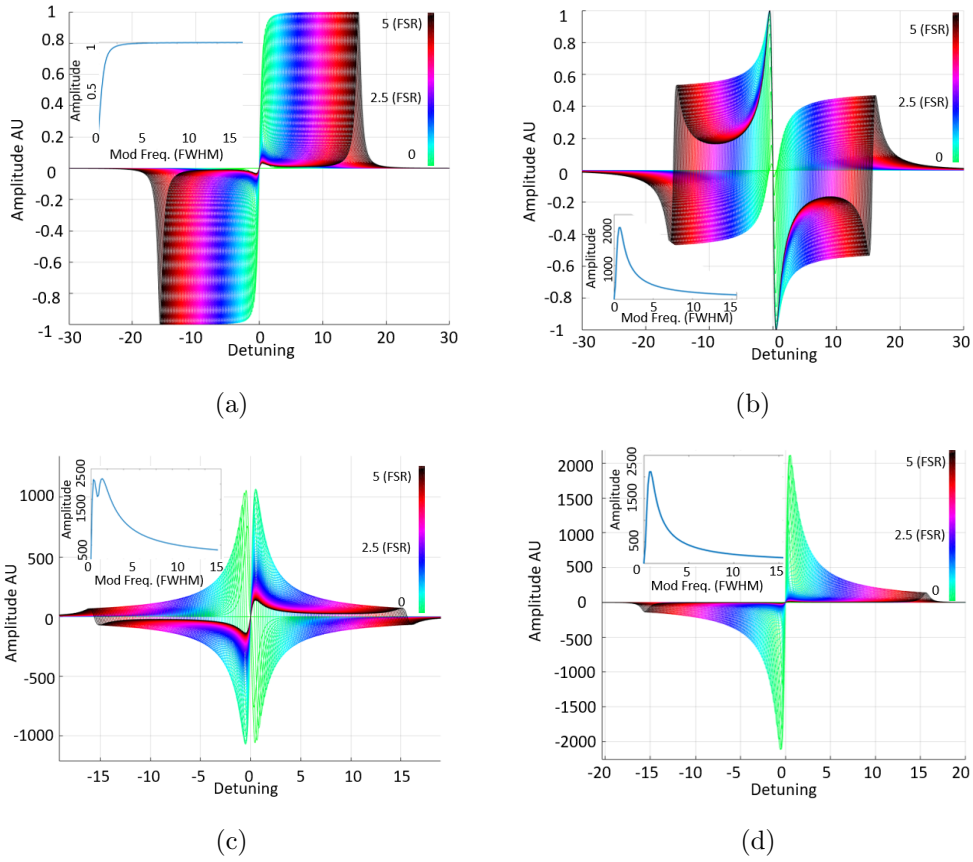

Figure 26: Simulated PDH error signal for a range of modulation frequencies, the insets show how the amplitudes vary for different Ω. a) Real component of error signal in reflection, b) imaginary component in reflection, c) real component in transmission, d) imaginary component in transmission.

3.5.3 Attempting to Lock in Transmission

The procedure for engaging the lock is as follows: as the cavity length is scanned by a FSR, the scan parameters are adjusted such that the amplitude of the waveform applied to the piezo is reduced. The amplitude is reduced further while manually adjusting the offset on the HVA to remain over the cavity linewidth. When the scan amplitude is effectively 0 V, we manually adjust the dc offset on the HVA to remain approximately at the resonance position. A transmission peak on the output signal is no longer observed but an offset corresponding to the transmission peak height is

present. The proportional and integral component of the feedback loop is engagned when the cavity is on resonance and the gain parameters are adjusted such that the system locks to the resonance position.

We initially observed that upon reducing the piezo scan amplitude ($\rightarrow$ 0 V), the resonance peak would fluctuate x10($\Delta\phi_{FWHM}$). It was evident that some source of noise was attributed to this. When manually adjusting the offset voltage on the piezo, one would expect to see an offset in the optical signal corresponding to the resonance position. Rather, a series of pulses due to the cavity briefly being on resonance was observed. The full width at half maximum of these pulses corresponded to a duration in the tens of microseconds which suggests that the cavity only remained on resonance for a few hundred nanoseconds, this suggests that the cavity is fluctuating in and out of resonance in the kHz range.

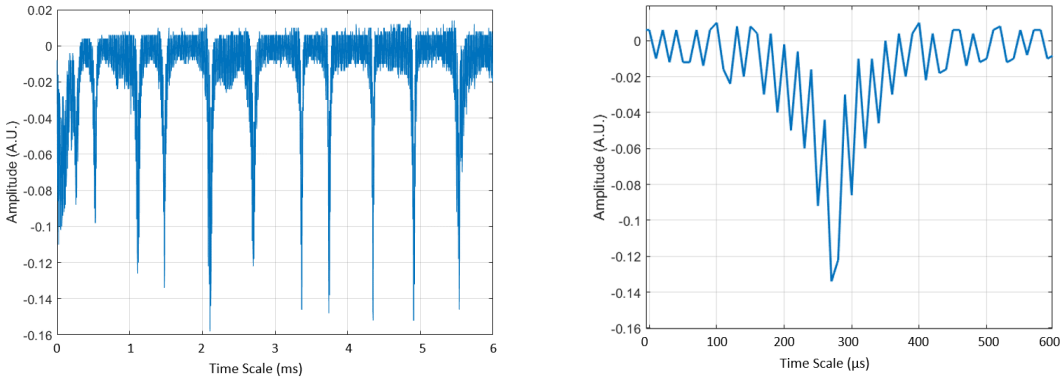

(a) (b)

Figure 27: a) Cavity transmission signal when the piezo is manually adjusted to the resonance position, the cavity is fluctuating in and out of resonance. b) A close up of a single trace of a resonance peak as the cavity is fluctuating, the cavity stays on resonance for approximately hundreds of ns.

By investigating sources of electrical and optical noise it was concluded that mechanical instabilities within the set-up was the source of this. These fluctuations (which shall be referred to here on as mechanical jitter) were eventually reduced by installing sorbathane isolators and enclosing the system in a closed wooden box which reduced

the mechanical jitter by a factor of two. However it appeared that the source of these mechanical instabilities were from the input fibre, in particular it seemed that the translation stage (TritorMini, T-401-00) in which the input fibre was mounted on was susceptible to acoustic vibrations. It has been observed in other studies that this particular stage has a medium-Q mechanical resonances in the low acoustic range [52]. The jitter was further reduced by clamping down all electrical and optical connections to prevent vibrations travelling to the system and clamping sorbathane to the translation stage. Despite the mechanical jitter now reduced to twice the $\Delta\phi_{FMWH}$, this ultimately reduces the amplitude of the fluctuations and does not increase the amount of time the cavity spends on resonance which was measured to be unchanged. Despite maximising the bandwidth of the components in the system, three root issues identified were ultimately a roadblock.

The first of which is that the feedback loop has to be engaged when the cavity is on resonance, given the narrow time frame in which the cavity remains on resonance ($\sim$200 ns), which is too brief for any of the components to engage in. The second, is that even if the feedback loop could be engaged on resonance, overall changes in the cavity position are too fast for the electronics in the feedback loop to successfully correct for, in particular the HVA is the slowest of components with a bandwidth of 200 kHz. The final issue is that despite only being able to observe changes in cavity position in 1D (along the cavity axis) through changes in cavity transmission intensity, the jitter was most probably in 3D. This is particularly plausible given that the source of the mechanical instability is most likely due to the translation stage. Furthermore, the locking scheme will not be able to correct changes in XYZ as the current set up feeds back to the shear piezo correcting only the cavity length (Z).

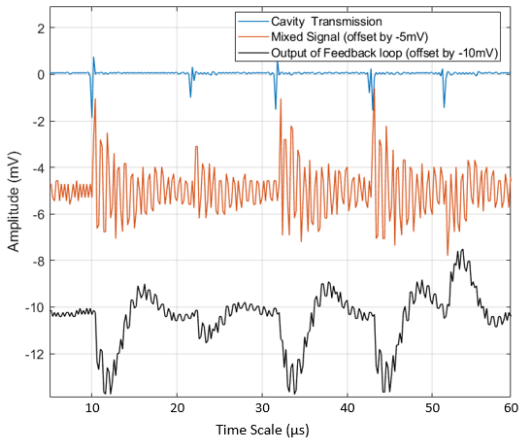

(a)

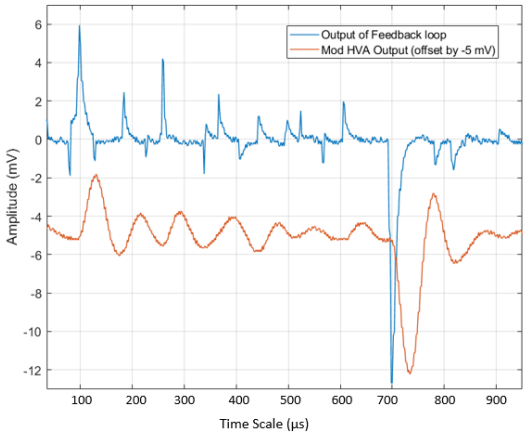

(b)

Figure 28: a) The signal from the cavity transmission, the mixer and the PI feedback loop showing the delay in response. b) The signal from the PI feedback loop and the HVA which feeds back to the shear piezo correcting the cavity length, the response delay of the HVA is particularly evident at 700 μs.

To determine whether or not the translation stage was the source of mechanical instabilities, this was replaced with a machined block. The v-groove that holds the fibre-electrode assembly is aligned and glued in place with a mechanical translation stage. While the epoxy cured, the cavity was iteratively aligned and the jitter on the cavity transmission signal was examined. No mechanical jitter was observed ($< \Delta\phi_{FMWH}$) and it was found that the cavity remains on resonance for ~ 2 ms. Which confirms that the piezo stage was the source of mechanical instability. However, upon unclamping the v-groove, it was found that cavity alignment was lost and with no means of correcting alignment, there was no way to lock the system.

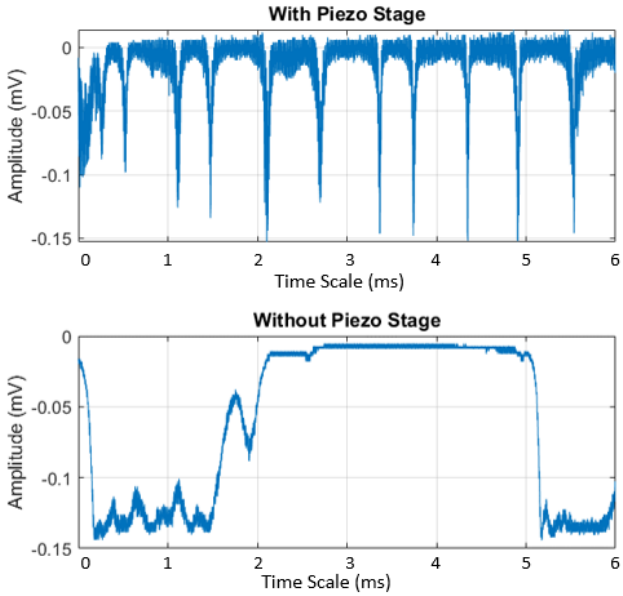

Figure 29: Cavity transmission signal when the piezo is manually adjusted to the resonance position, we observe that the cavity remains on resonance for much longer (> 1 ms) when the translation stage is substituted with a solid block.

3.6 Conclusion

A test set up that replicates the cQED endcap design presented in Chapter 2 was built. The new design maximises optical access and aimed at delivering a more robust lock by improving the mechanical rigidity of the overall system. A PDH locking system was employed to verify this however, generating an error signal in reflection was troublesome. This was due to the fibres that comprised the cavity were not polarisation maintaining, and a lack of interference of the reflected light and the input beam did not yield an error signal in reflection. Nonetheless, despite a reduced locking bandwidth, generating an optimised error signal in transmission was possible.

It was later observed that prior to engaging the feedback loop, mechanical noise was causing our cavity to go in and out of resonance on a time scale that was out of the bandwidth of any of the components. This was ultimately due to the translation stage (TritorMini, T-401-00) used for fine cavity alignment. It was observed that upon replacing this stage with a machined block the cavity was able to remain on resonance on the order of milliseconds which would have been enough time for the feedback loop to engage and lock the cavity. However, a misalignment when dismounting rendered the system defective beyond further testing.

A 3D translation stage to maximise optical access whilst allowing for fine adjustments in cavity alignment was used. An alternative would be to machine a monolithic system in which no moving parts are present. However to correct for minute errors in the mounting and glue curing process would add a layer of complexity to the system. Furthermore, the tolerances with which a monolithic system could be machined to was a further limitation.

After much consideration, the use of fibre based cavities were deemed too problematic. Instead, miniature free space cavities were opted for. The designs for a linear microtrap system that uses free space cavity mirrors in the following chapter are presented.

4 A Linear Microfabricated Trap

4.1 Introduction

Thus far, the focus of this dissertation was on developing an endcap Paul trap capable of strong coupling. As discussed, the design was developed by further iterating on the design used in [28]. However, as was observed the use of fibre cavities uncovered a number of unavoidable technical challenges. In a new design presented here, fibre cavities are not used and instead free space cavities will be implemented. In this chapter the initial design for a linear microfabricated Paul trap is presented. Unlike the endcap design discussed in Chapter 2, this system will have the ability to trap strings of ions. The trap will feature a segmented architecture with different trapping regions reserved for different purposes. There are four different regions; loading, storage, computation and communication. The storage segment will be used to keep a reservoir of ions, loaded from the atomic oven. The reservoir will be a string of ions which can be selectively shuttled from this reservoir into the computation node reserved for gate operations. The final node being the communication node which will rely not on fibre based cavities but will use micrometer free space cavities. The benefit of using these is that they are able to provide small mode volumes (the main benefit behind fibre cavities) while allowing external mode matching optics to be implemented while circumventing the issues discussed in Chapter 3. Prior to fabricating the components of the trap, an understanding of the trapping dynamics is required to optimise the splitting protocol. To this end, the trapping dynamics under different electrode dimensions are simulated. It begins first by simulating the rf dynamics radially and axially to optimise the electrode dimensions, then the preliminary results of the splitting protocol are presented.

4.2 Proposed Design

Linear segmented traps have been a popular choice for scalable trapped ion quantum processors, [5, 53, 54]; these systems can trap several ions and can be built using methods of microfabrication or laser machining and have been a popular architecture for QCCD based devices first mentioned in chapter 1.1.

This design is an initial iteration developed by M.Keller and adopts a three-dimensional blade-shape-electrode configuration in which each blade features segmented electrodes perpendicular to the trap axis that provide axial dc confinement. These electrodes will be used to shuttle and transport ions along the trapping axis. And will also feature an rf tip that runs parallel to the trap axis and will be used to provide the main rf trapping field. Each blade is composed of a sapphire substrate with gold electrodes. The four blades will be mounted at right angles to each other and held by a mounting structure.

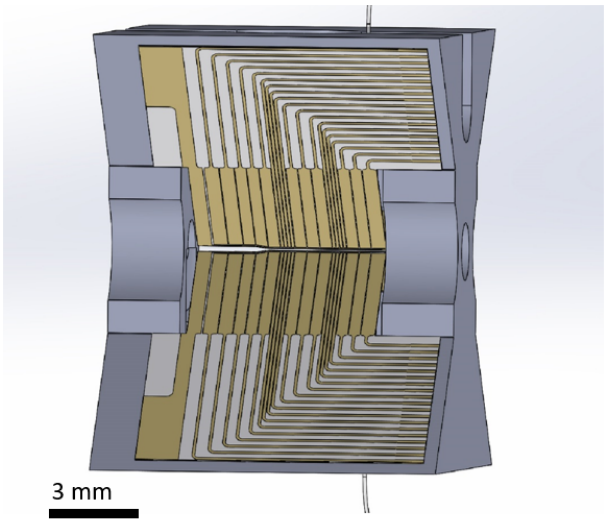

(a)

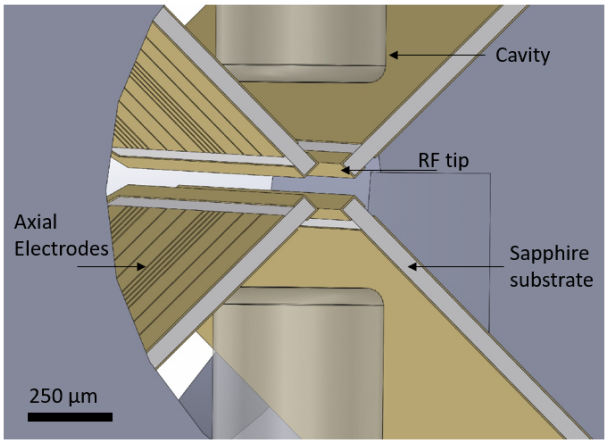

(b)

Figure 30: a) CAD image of the linear micro-trap, showing the plane of optical access. b) A close up of the communication/cavity segment showing the cavities and the four perpendicular blades.

To maximise optical access the atomic oven and cavity mounting structure are shielded from the main area of optical access. The electrode dimensions will vary depending on their function. In the loading region electrode-ion separation is larger than in other areas, this is to reduce contaminating the electrodes with calcium during the loading process. The widths of the axial electrodes can be adapted to optimise the splitting process, similarly for the computation segment; the electrode dimensions can be optimised to carry out gate specific operations that require control over motional degrees

of freedom.

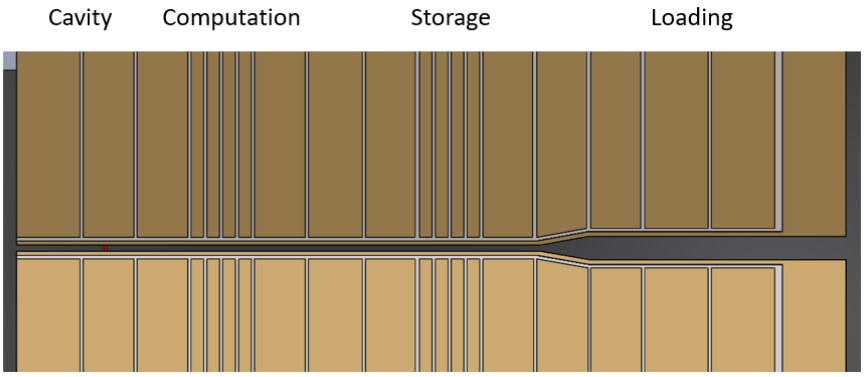

Figure 31: The proposed arrangement for the axial segmented electrodes highlighting the varying dimensions specific to their operations.

4.3 rf Simulations

In this subsection, the same finite element simulation model (COMSOL Multiphysics) used in simulating the trapping dynamics in chapter 2 is adopted to optimise the electrode dimensions. Our initial test was to vary the electrode-ion (trap centre) separation and to observe the effect this had on the pseudopotential and optical access. The effect of varying the amplitude on two neighbouring electrodes was also varied to observe the effect this has on the position of the potential minimum radially, this is so that the ion's position can be shifted.

4.3.1 rf Electrode Geometry

To maintain a small cavity mode volume (L & $R_{curvature} \approx 500\ \mu m$) while shielding the ion from the dielectric interference of the cavity mirrors, the approach adopted is the one used in [49] and in chapter 2 in which the cavity is retracted away from the rf field, effectively shielding the trapping region from the cavity facet. Increasing the separation between our electrodes would increase optical access to the ion. Doing so however, would limit the shielding of the ion from the dielectric surface of the cavity which would effect the potential. The effect this has on the trap depth is observed and

by fitting a second order polynomial to the potential, the coefficient of the quadratic term is extracted and secular frequencies for different electrode-ion separations are calculated.

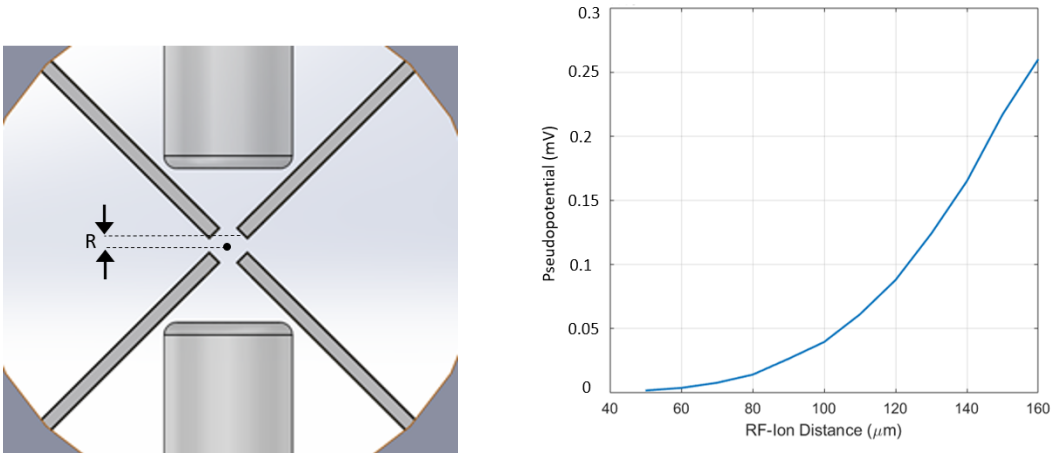

(a) (b)

Figure 32: a) Schematic of the electrode-ion separation (R) distance shielding the potential from the cavity. b) The effect of varying the rf electrode-ion separations on the value of the pseudopotential at the trap centre with an rf voltage of $V_{rf} = 1$ V and trap drive frequency $\Omega_{rf} = 20$ MHz .

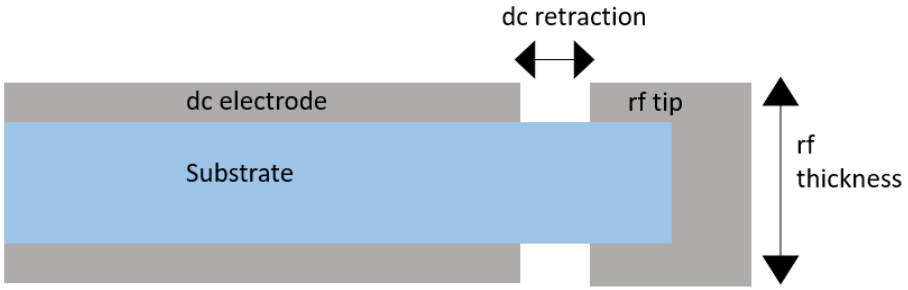

Figure 33: Schematic of the cross section of the electrode structure

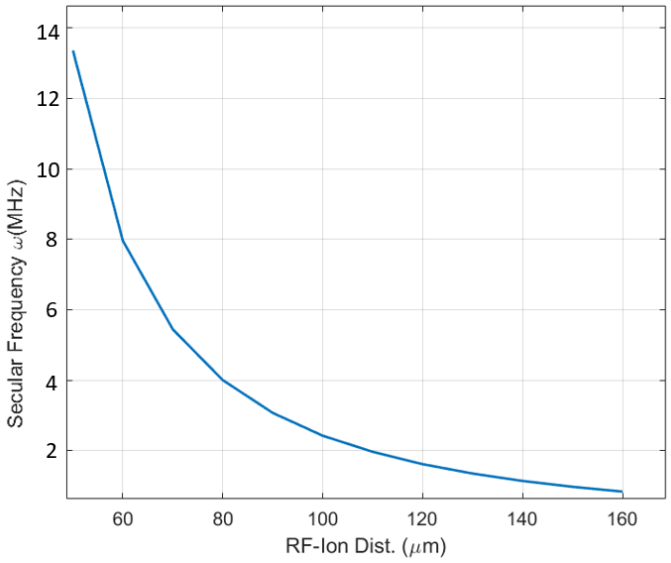

Figure 34: The effect of varying the rf electrode-ion separation on the ion's secular frequency, for which they exponentially decrease.

For the purpose of the next simulations the electrode-ion separation is arbitrarily set at 110 μm, this value was selected as it was found to be a balance between a reasonable value of secular frequency and to maximise optical access. To further increase optical access the thickness of the rf electrode tip is varied (fig 35). A minimal change in secular frequency ($<$ 100 kHz) is observed.

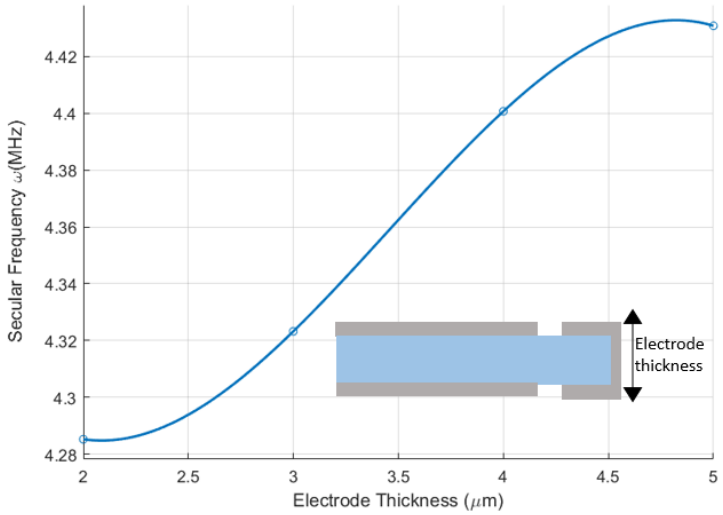

Figure 35: The effect of reducing the rf electrode thickness on the ion's secular frequency.

Ideal Trap Frequency

The expected theoretical value of the radial secular frequency can be determined from the following expression

$$\omega_{\mathrm{rf}} = \frac{\sqrt{\frac{q^2}{2} + a}}{2}\Omega, \tag{44}$$

where a and q are the stability parameters axially and radially respectively, first mentioned in chapter 2.2.1. The radial stability is given by

$$q = \frac{2QV_{\mathrm{ac}}}{Mr^2\Omega^2}, \tag{45}$$

where Ω is our trap drive frequency. As the ion's radial position is of interest in this simulation, dc potentials are set to null and hence the a value is negligible, the secular frequency is dependent on the rf amplitude. Based on a peak to peak rf voltage of 2 V and an r = 110 μm and a trap drive frequency (Ω = 20 MHz). An ideal secular frequency of 2.24 MHz was calculated from (13) and a secular frequency of 2.09 MHz is observed from the simulations. From this the ideal trap frequency can be calculated by simply taking the ratio of the two values. A trap efficiency of 88% was observed.

4.3.2 Positioning the Ion with rf

Precisely controlling the ion's position radially to the cavity mode is crucial in maximising the ion-cavity coupling. Where previously the trap potential was perturbed with grounded side-electrodes, in this linear trap this is done solely by increasing the amplitude of two neighbouring pairs of rf electrodes, thus changing the trap depth on one side. In this model the rf amplitude are increased on two electrodes from 1 V to 2 V.

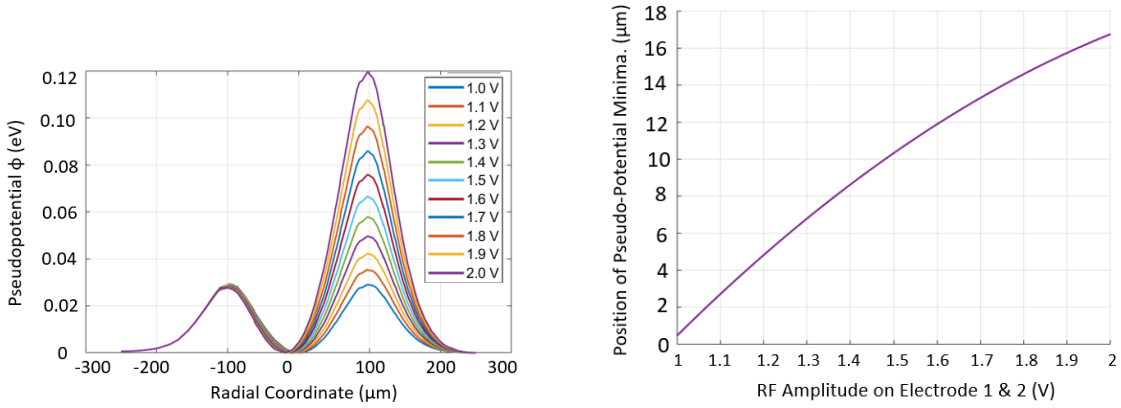

(a)

Figure 36: a) Simulated radial pseudopotential, the potential falls sharply due to the presence of the blade electrodes at $\sim 100\,\mu$m, as the amplitude is increased on two electrodes this corresponds to an increase in the trap depth. b) The position of the pseudopotential minimum for increasing values of rf amplitude on two electrodes.

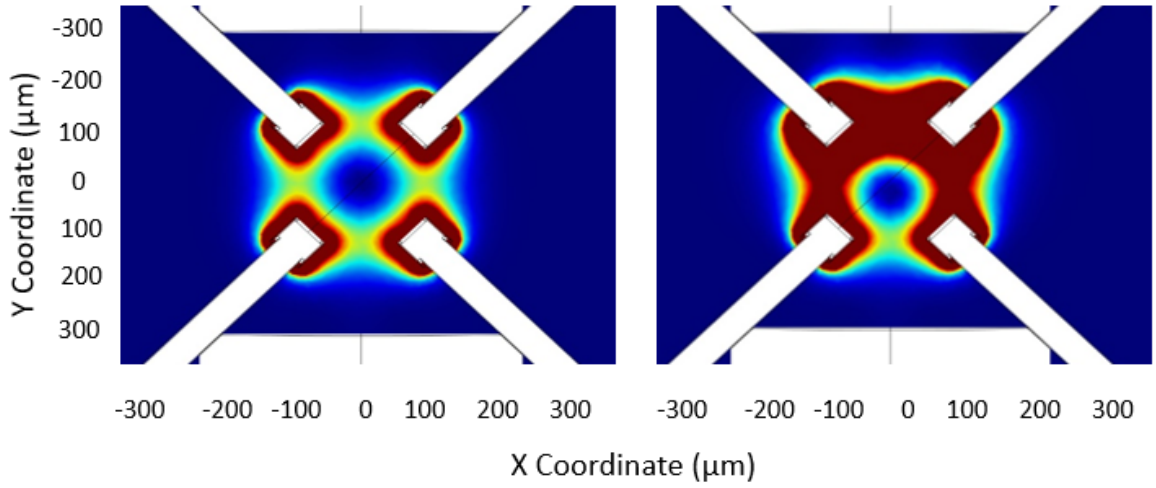

Figure 37: 2D slice showing the distribution of the potential around the electrodes along the trapping axis (Z). Left: with equal amplitudes on all electrodes. Right: the pseudopotential when the amplitude on the top two electrodes are increased to 2 V.

By increasing the amplitude of two electrodes to 1.7 V yields a shift in the potential minimum of 20 μm is observed.

The ion's secular frequency is computed and hence its q value to observe if the ion remains in the acceptable stable region radially, $(0.1 < q < 0.9)$. As the asymmetry of the rf amplitude increases, a linear increase of the secular frequency and hence the q

value is observed. The q value remains within the stable region.

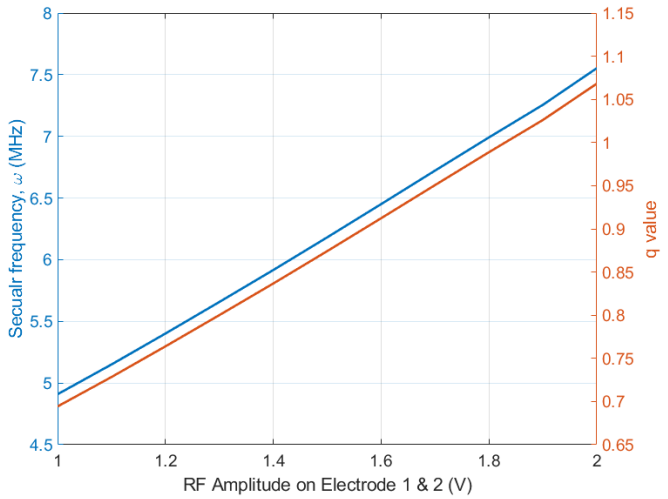

Figure 38: The linear increase of secular frequency and q value as the pseudopotential minimum is shifted for $V_{ac} = 1$ V-2 V, $\Omega_{ac} = 20$ MHz.

It has been deemed that a suitable electrode-ion spacing that does not interfere with our trapping potential is $75 - 110$ μm, within this range simulated secular frequencies are (2-4) MHz. By reducing the thickness of the rf electrode tips, optical access is increased without compromising the ion's stability. Additionally it was determined that by doubling the amplitude of two neighbouring electrodes, the pseudopotential minimum is shifted by $\sim$18 μm.

4.4 Axial Trapping Dynamics

Unlike the endcap trap studied in chapter 2 where a single ion was localised to a single minima along the trapping axis, this linear segmented configuration will entail that multiple ions are shuttled along the trapping axis. Hence, this section is dedicated to studying the axial trapping behaviour of the system and to optimising the axial dc electrodes. As stated previously a key aspect of the new trap is the ability to control the axial potential such that we are able to selectively move a single ion from a string of stored ions. This will be done by varying the dc potential on the axial segmented

electrodes, such that a chain of ions can be split coherently, or selectively shuttle one ion off a string of multiple ions. In principle this is done by wedging a parabolic (x^2) potential into a quartic potential (x^4) which will effectively 'split' our chain of ions. In order to simulate this splitting behaviour, a simulation of a single well pseudopotential in the axial plane is done. Multiple single well potentials are combined to form a double well potential, the results generated will then be used with a model that simulate the dynamics of calcium ions in a potential.

4.4.1 dc Electrode Geometry and Trapping Dynamics

The axial potential from a single segment of three electrodes is simulated in this sub-chapter. The central electrode is set to some dc voltage and the outer electrodes are grounded. The electrodes are on a dielectric (insulator) substrate, their widths are varied and their distance from the rf electrode are increased. The varied widths are in a range of (50 - 800) μm, in order to observe the effect this has on the shape of the pseudopotential; the linewidths of the potentials are measured along with the ion's secular frequency. By doing so, broader linewidths with wider minima are observed as the electrode widths are increased. The broader linewidths would suggest a decrease in confinement i.e. decrease in secular frequency. The distance between the dc electrodes and the rf are also varied and the effect this has on the secular frequency and stability is observed.

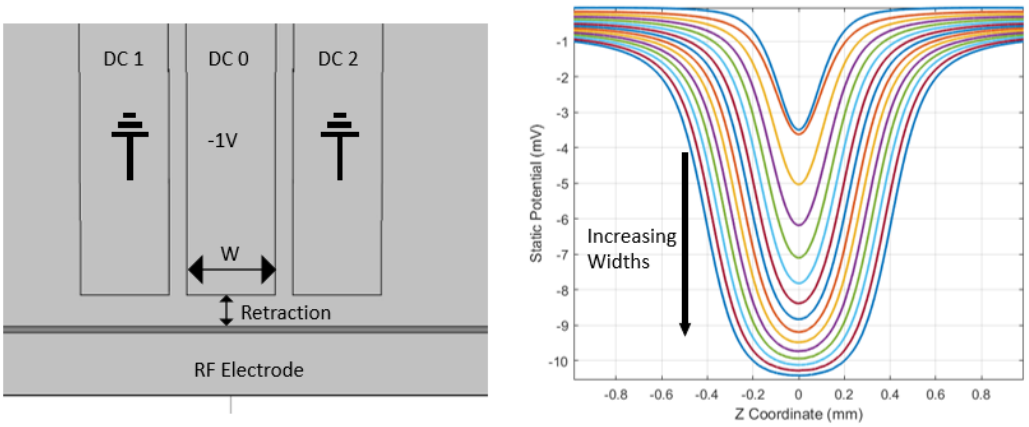

Figure 39: Left: Schematic of the simulated electrode configuration Increasing the width (W) of electrode DC 0, where W = (50 - 800) μm.

The ion's secular motion is maximal at widths (100-200) (μm)

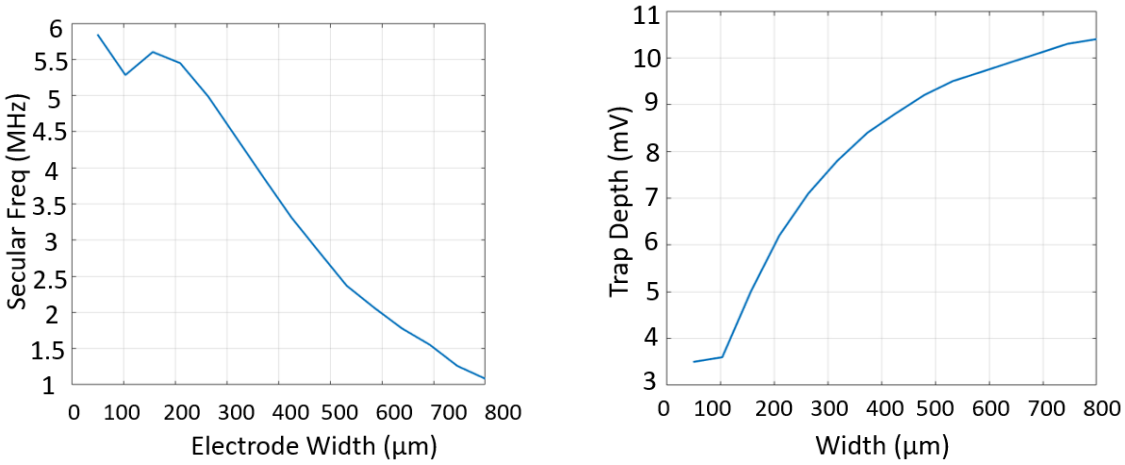

(a) (b)

Figure 40: The effect of varying the electrode width on a) secular frequency, b) trap depth. The cause of the kink observed at electrode width = 100 μm for both plots is not fully understood.

When retracting the dc electrode away from the rf, a linear decrease in the trap depth is observed as well as a decrease in secular frequency.

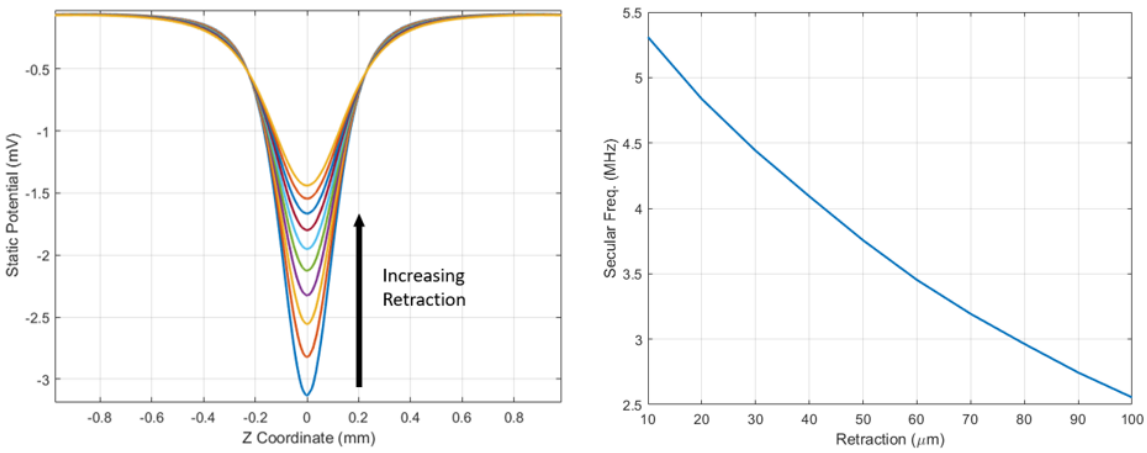

Figure 41: The effect of varying the electrode retraction on a) the potentials b) secular frequency.

The linear decrease in trap depth causes a decrease in trap confinement as the electrode is retracted away from the ion. This is attributed to the fact the electric field of a point charge follows an inverse square law, which is observed in the decay of the secular frequency. With the range of potential shapes obtained from the above simulations, a particular electrode dimension is selected to be used in the simulation of two ion splitting, these dimensions will be determined in the following subchapter by observing how the quartic component of our line shapes varies as the potential evolves.

4.5 Splitting an Ion Crystal

Shuttling ions in Paul traps has been a promising means of manipulating and controlling qubits. In particular for transporting ions into the different regions of an ion trap reserved for different tasks such as storage and for processing. Shuttling through different arrays has been successfully demonstrated [55, 56, 57]. In every case, configuring the electrode geometry and optimising the shuttling parameters has been crucial in working towards adiabatic transport. Splitting ions in an rf Paul trap was first demonstrated in [56] and the general case of optimising electrode structure for ion crystal splitting has been outlined in [58]. It has been noted that a challenge is that the harmonic part of

the potential defined by α has to cross some critical point when $\alpha \to 0$ where the ion's confinement is at it's lowest.

In this chapter the preliminary work in simulating and studying the splitting dynamics in our 3D segmented trap structure is presented. It begins by generating a double well potential from the single wells simulated above. The different potential shapes are implemented in a full 3D dynamical model that simulates the Coulomb repulsion, the force due to the potential and an external force that represents some damping due to laser cooling.

4.5.1 The Quartic Component

Thus far the case of a single trapped ion is presented. However, for the simplest case of splitting two ions, some static voltage that transforms the single well into a double well is applied. Mathematically, the potential goes from being a quadratic (x^2) to a quartic (x^4), the potential is of the form

$$\Phi(x) \approx \beta x^4 + \alpha x^2 + \gamma x. \tag{46}$$

where β, α, γ are defined by the trap geometries. As the potential evolves from a single well ($\alpha_i > 0$) to a double well ($\alpha_f < 0$) the potential passes a critical point, $\alpha = 0$ in which the potential minimum become flat. It is required that $\beta > 0$ when $\alpha \leq 0$. At the critical point, harmonic confinement vanishes and a weak residual confinement is preserved from a combination of the coloumb repulsion of the two ions and the quartic term of the confining potential. Hence ensuring that β is maximised at $\alpha = 0$ is essential for the splitting process.

The force due to the potential (46) in z is expressed as

$$\frac{\partial \phi}{\partial z} = 2\alpha + 4\beta z^3. \tag{47}$$

When $\alpha < 0$, the defined equilibrium position of $z = \sqrt{\frac{|\alpha|}{2\beta}}$, the secular frequency is expressed as

$$\omega = \sqrt{\frac{4q \mid \alpha \mid}{m}}. \tag{48}$$

Similarly following the steps in [58], for $\alpha \to 0$, the position of the potential minimum is

$$z \simeq \left(\frac{e}{2\pi\epsilon_0\beta}\right). \tag{49}$$

At this critical point the secular frequency is at its minimum and the dominant force acting on our ions is due to the coulomb repulsion, the secular frequency is expressed as

$$\omega_{min} = \sqrt{\frac{3e}{m}}\left(\frac{e}{2\pi\epsilon_0}\right)^{1/5}\beta^{3/10}. \tag{50}$$

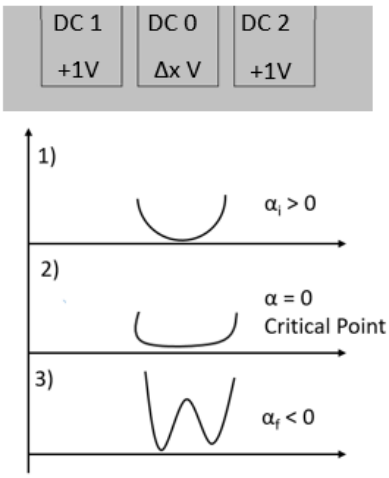

Figure 42: The evolution of the potential from a quadratic ($\alpha < 0$) to the critical point ($\alpha = 0$) to a quartic potential ($\alpha > 0$). This is driven by the voltage on DC 0 being ramped from -1V to +1V.

The splitting process is driven by varying the voltage on the central electrode (DC 0), to simulate the evolution of the quartic component, a single well potential from the

parameters optimised above are combined and applied to three electrodes; the central electrode (DC 0) and the left and right segments (DC 1 & DC 2). The summation of three single welled (parabolic) potential results in the double well (quartic) potential. For these simulations to maximise shielding of the cavity, the rf-ion separation is reduced to 75 μm.

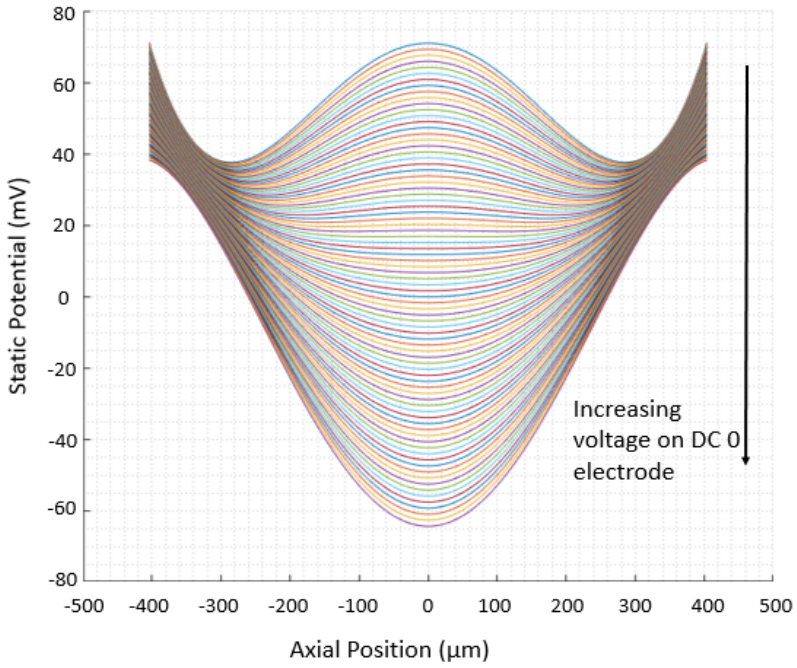

Figure 43: The sum of three quadratic potentials yielding a quartic potential for an increasing voltage on the central segment (DC 0), it is observed that the critical point occurs when the shape of the potential at the minimum is flat.

The coefficients that define the shape of each potential based on the electrode variations are extracted. As it is desirable to maximise the quartic component at the critical point, the electrode width that yields the highest secular frequency was found. For an electrode separation of 10 μm, it was deemed that β is maximised for an electrode width of 270 μm.

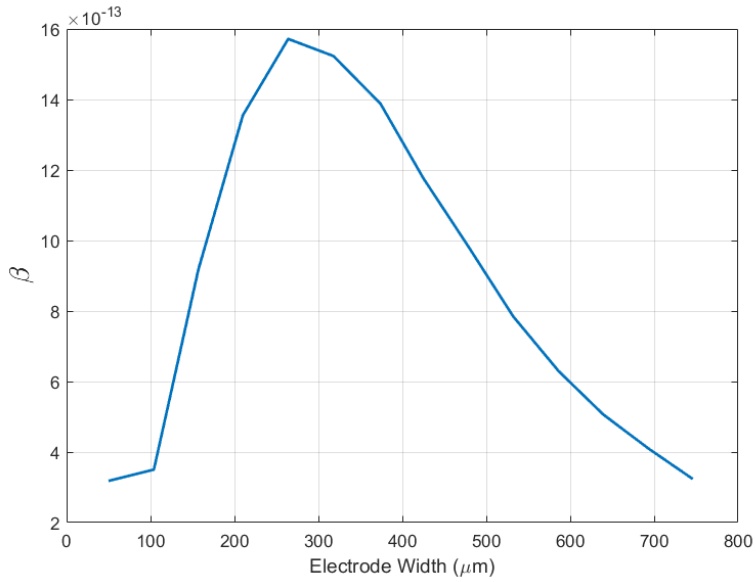

Figure 44: The quartic component (β) at the critical point for different central electrode (DC 0) widths. The optimal value occur about 270 μm.

4.5.2 Molecular Dynamics Simulations

Previously, the pseudopotentials for a single well transforming into a double well were simulated. In this section, the preliminary stages of simulating the splitting protocol is presented. This is done by plotting the ion's position for varying potential shapes in a full 3D model. The model is driven by two forces; the force due to the coulomb repulsion and the force due to the potential. The driving factor in this model is the changing force due to the potential transforming from a quadratic to a quartic for a central electrode width of W = 270 μm. As the ion is initially in a single well, their separations are at $z = 0$. As the potential reaches the critical point, the coulomb repulsion becomes the dominant force causing the separation between the two ions to increase (time evolution = 30). As β increases a wedge is formed between the two ions and once again the dominating forces are due to the potential. The two ions are separated into two wells and oscillate about their respective equilibrium positions (at time evolution = 60). The final separation of the two ions corresponds to the position of the double wells $\pm$250 μm.

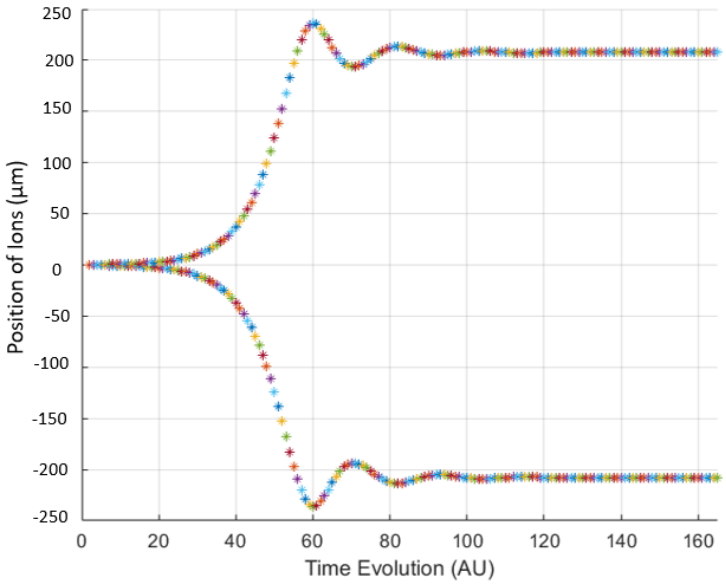

Figure 45: The splitting of two ions in a quartic potential, configured for an initial position of z = 0 (the centre of the wedge), the ions move away from each other due to coulomb repulsion, they then oscillate about the potential minimum or each well at a separation of $\sim 200\ \mu$m.

This marks the preliminary stage of a full simulation of the dynamics of the splitting of ion chains. To fully evaluate the performance of the splitting protocol, the heating rate of the ion while the potential evolves is to be determined. The ion is particularly susceptible to effects due to anomalous heating. Such occurs when the mean phonon number increases due to thermalisation with electrons at scales much greater than the electronic noise generated by the thermal agitation of charge carriers.

5 Conclusion & Outlook

The original motivation of this work was to develop a cavity QED system in which a single ion could be coupled to the modes of an optical cavity and demonstrate not only strong coupling but a deterministic entanglement scheme that would form the basis for a network of trapped ion processors. To this end an endcap system with a fibre based cavity was deemed the most ideal system given the previous success of a similar endcap system, the first of which to achieve strong coupling between a single ion and an optical cavity.

An improved system based off the one used by Takahashi et al. was designed; one that would feature a number of improvements over the previous generation of the end cap fibre cavity trap. The design featured greater optical access by using different electrode materials and dimensions, this was facilitated with an improved insertion technique. Optically, the system would feature greater mode matching with the cavity mode and fibre mode by using a concatenated assembly of GRIN and SM fibres.The trap would also feature a novel means of adjusting the ion's position radially to optimise ion-cavity coupling. This was proposed by distorting the pseudopotential by mechanically adjusting the position of grounded side electrodes. Simulations results showed that the travel of the stage controlling the position of the electrodes would be enough to correct for the eccentrics incurred during the insertion stage (~ 6 μm).

A crucial part of developing a cavity QED system was the stability of the cavity. Of great hindrance to the previous generation was the cavity's inability to stay on resonance in response to acoustic noise. This was attributed to the limited bandwidth of the cavity locking scheme due to relying on an error signal in transmission rather than reflection and the overall mechanical structure surrounding the system. Our design aimed at

addressing these issues however we were unsuccessful in locking our system using the PDH method. It was observed that mechanical noise inherent in the system inhibited this. The noise was eventually reduced by a factor of 10 by adding dampers such as sorbathane isolators or clamping down any lose electrical/optical connections that were directly coupled to the system. However it was observed that the cavity would remain on resonance for a brief period of time $\sim$ 100 ns, which was too brief for our feedback loop to correct for. It was concluded that the stage used to finely adjust cavity alignment was the source of the mechanical noise. The alternative would be to design a monolithic system however it was deemed infeasible.

It was then decided to develop a linear micro trap, one that could trap a string of ions that could demonstrate not only cQED but also gate operations. The preliminary design features different regions reserved for operations related to ion-photon entanglement and gate operations. A novel feature being the ability to selectively load single ions from the stored reservoir. Prior to fabrication, simulations to determine the optimal electrode dimensions were carried out. The simulations maximised secular frequency in both axial and radial dimensions, stability parameters a & q found to be within stable ranges. In particular, it was determined that a dc electrode width of $\sim$ 270 μm would yield the highest quartic component at the critical point. Further development of the simulations to fully evaluate the heating rate of the ion and optimise the splitting procedure is required. This would entail dynamic simulations of the potential varying in time under some external damping (laser cooling) force. It is evident that further work is required for the development of this system both on the simulation front and the apparatus. The work presented in this section outlines only the preliminary stages for further development.

References

[1] P. W. Shor, "Algorithms for quantum computation: discrete logarithms and factoring," in *Proceedings 35th annual symposium on foundations of computer science*. Ieee, 1994, pp. 124–134.

[2] D. P. DiVincenzo, "The physical implementation of quantum computation," *Fortschritte der Physik*, vol. 48, no. 9-11, p. 771–783, Sep 2000. [Online]. Available: http://dx.doi.org/10.1002/1521-3978(200009)48:9/11⟨771::AID-PROP771⟩3.0.CO;2-E

[3] Y. Wang, M. Um, J. Zhang, S. An, M. Lyu, J.-N. Zhang, L.-M. Duan, D. Yum, and K. Kim, "Single-qubit quantum memory exceeding ten-minute coherence time," *Nature Photonics*, vol. 11, no. 10, pp. 646–650, 2017.

[4] A. Myerson, D. Szwer, S. Webster, D. Allcock, M. Curtis, G. Imreh, J. Sherman, D. Stacey, A. Steane, and D. Lucas, "High-fidelity readout of trapped-ion qubits," *Physical Review Letters*, vol. 100, no. 20, p. 200502, 2008.

[5] G. Wilpers, P. See, P. Gill, and A. G. Sinclair, "A monolithic array of three-dimensional ion traps fabricated with conventional semiconductor technology," *Nature nanotechnology*, vol. 7, no. 9, p. 572, 2012.

[6] H. J. Kimble, "The quantum internet," *Nature*, vol. 453, no. 7198, p. 1023–1030, Jun 2008. [Online]. Available: http://dx.doi.org/10.1038/nature07127

[7] M. Lee, K. Friebe, D. A. Fioretto, K. Schüppert, F. R. Ong, D. Plankensteiner, V. Torggler, H. Ritsch, R. Blatt, and T. E. Northup, "Ion-based quantum sensor for optical cavity photon numbers," *Phys. Rev. Lett.*, vol. 122, p. 153603, Apr 2019. [Online]. Available: https://link.aps.org/doi/10.1103/PhysRevLett.122.153603

[8] P. Kómár, E. M. Kessler, M. Bishof, L. Jiang, A. S. Sørensen, J. Ye, and M. D. Lukin, "A quantum network of clocks," *Nature Physics*, vol. 10, no. 8, p. 582–587, Jun 2014. [Online]. Available: http://dx.doi.org/10.1038/nphys3000

[9] M. Sasaki, M. Fujiwara, H. Ishizuka, W. Klaus, K. Wakui, M. Takeoka, S. Miki, T. Yamashita, Z. Wang, A. Tanaka, and et al., "Field test of quantum key distribution in the tokyo qkd network," *Optics Express*, vol. 19, no. 11, p. 10387, May 2011. [Online]. Available: http://dx.doi.org/10.1364/OE.19.010387

[10] J. Yin, Y. Cao, Y.-H. Li, S.-K. Liao, L. Zhang, J.-G. Ren, W.-Q. Cai, W.-Y. Liu, B. Li, H. Dai *et al.*, "Satellite-based entanglement distribution over 1200 kilometers," *Science*, vol. 356, no. 6343, pp. 1140–1144, 2017.

[11] V. Krutyanskiy, M. Meraner, J. Schupp, V. Krcmarsky, H. Hainzer, and B. Lanyon, "Light-matter entanglement over 50 km of optical fibre," *npj Quantum Information*, vol. 5, no. 1, pp. 1–5, 2019.

[12] D. Hunger, T. Steinmetz, Y. Colombe, C. Deutsch, T. W. Hänsch, and J. Reichel, "A fiber fabry–perot cavity with high finesse," *New Journal of Physics*, vol. 12, no. 6, p. 065038, jun 2010. [Online]. Available: https://doi.org/10.1088\%2F1367-2630\%2F12\%2F6\%2F065038

[13] M. Keller, B. Lange, K. Hayasaka, W. Lange, and H. Walther, "Continuous generation of single photons with controlled waveform in an ion-trap cavity system," *Nature*, vol. 431, no. 7012, pp. 1075–1078, 2004.

[14] A. Narla, S. Shankar, M. Hatridge, Z. Leghtas, K. M. Sliwa, E. Zalys-Geller, S. O. Mundhada, W. Pfaff, L. Frunzio, R. J. Schoelkopf *et al.*, "Robust concurrent remote entanglement between two superconducting qubits," *Physical Review X*, vol. 6, no. 3, p. 031036, 2016.

[15] Y. Wang, Y. Li, Z.-q. Yin, and B. Zeng, "16-qubit ibm universal quantum computer can be fully entangled," *npj Quantum Information*, vol. 4, no. 1, pp. 1–6, 2018.

[16] R. Courtland, "Google aims for quantum computing supremacy [news]," *IEEE Spectrum*, vol. 54, no. 6, pp. 9–10, 2017.

[17] F. Arute, K. Arya, R. Babbush, D. Bacon, J. C. Bardin, R. Barends, R. Biswas, S. Boixo, F. G. Brandao, D. A. Buell *et al.*, "Quantum supremacy using a programmable superconducting processor," *Nature*, vol. 574, no. 7779, pp. 505–510, 2019.

[18] C. Monroe and J. Kim, "Scaling the ion trap quantum processor," *Science*, vol. 339, no. 6124, pp. 1164–1169, 2013.

[19] J. I. Cirac and P. Zoller, "Quantum computations with cold trapped ions," *Physical review letters*, vol. 74, no. 20, p. 4091, 1995.

[20] C. Ballance, T. Harty, N. Linke, M. Sepiol, and D. Lucas, "High-fidelity quantum logic gates using trapped-ion hyperfine qubits," *Physical review letters*, vol. 117, no. 6, p. 060504, 2016.

[21] D. Kielpinski, C. Monroe, and D. J. Wineland, "Architecture for a large-scale ion-trap quantum computer," *Nature*, vol. 417, no. 6890, pp. 709–711, 2002.

[22] S. M. Clark, D. Hucul, I. V. Inlek, G. Vittorini, C. Crocker, S. Debnath, and C. Monroe, "Modular entanglement of atomic qubits using both photons and phonons." Sandia National Lab.(SNL-NM), Albuquerque, NM (United States), Tech. Rep., 2014.

[23] C. Nölleke, A. Neuzner, A. Reiserer, C. Hahn, G. Rempe, and S. Ritter, "Efficient teleportation between remote single-atom quantum memories," *Physical review letters*, vol. 110, no. 14, p. 140403, 2013.

[24] C. Monroe, R. Raussendorf, A. Ruthven, K. Brown, P. Maunz, L.-M. Duan, and J. Kim, "Large-scale modular quantum-computer architecture with atomic memory and photonic interconnects," *Physical Review A*, vol. 89, no. 2, p. 022317, 2014.

[25] K. Wright, K. M. Beck, S. Debnath, J. M. Amini, Y. Nam, N. Grzesiak, J.-S. Chen, N. C. Pisenti, M. Chmielewski, C. Collins, and et al., "Benchmarking an 11-qubit quantum computer," *Nature Communications*, vol. 10, no. 1, Nov 2019. [Online]. Available: http://dx.doi.org/10.1038/s41467-019-13534-2

[26] H.-J. Briegel, W. Dür, J. I. Cirac, and P. Zoller, "Quantum repeaters: the role of imperfect local operations in quantum communication," *Physical Review Letters*, vol. 81, no. 26, p. 5932, 1998.

[27] J. I. Cirac, P. Zoller, H. J. Kimble, and H. Mabuchi, "Quantum state transfer and entanglement distribution among distant nodes in a quantum network," *Physical Review Letters*, vol. 78, no. 16, p. 3221, 1997.

[28] H. Takahashi, E. Kassa, C. Christoforou, and M. Keller, "Strong coupling of a single ion to an optical cavity," *Physical Review Letters*, vol. 124, no. 1, Jan 2020. [Online]. Available: http://dx.doi.org/10.1103/PhysRevLett.124.013602

[29] C. Law and H. Kimble, "Deterministic generation of a bit-stream of single-photon pulses," *Journal of Modern Optics*, vol. 44, no. 11-12, pp. 2067–2074, 1997.

[30] H. Takahashi, E. Kassa, C. Christoforou, and M. Keller, "Cavity-induced anticorrelated photon-emission rates of a single ion," *Phys. Rev. A*, vol. 96, p. 023824, Aug 2017. [Online]. Available: https://link.aps.org/doi/10.1103/PhysRevA.96.023824

[31] L.-M. Duan and C. Monroe, "Colloquium: Quantum networks with trapped ions," *Rev. Mod. Phys.*, vol. 82, pp. 1209–1224, Apr 2010. [Online]. Available: https://link.aps.org/doi/10.1103/RevModPhys.82.1209

[32] D. L. Moehring, P. Maunz, S. Olmschenk, K. C. Younge, D. N. Matsukevich, L.-M. Duan, and C. Monroe, "Entanglement of single-atom quantum bits at a distance," *Nature*, vol. 449, no. 7158, pp. 68–71, 2007.

[33] B. Casabone, A. Stute, K. Friebe, B. Brandstätter, K. Schüppert, R. Blatt, and T. E. Northup, "Heralded entanglement of two ions in an optical cavity," *Phys. Rev. Lett.*, vol. 111, p. 100505, Sep 2013. [Online]. Available: https://link.aps.org/doi/10.1103/PhysRevLett.111.100505

[34] L. J. Stephenson, D. P. Nadlinger, B. C. Nichol, S. An, P. Drmota, T. G. Ballance, K. Thirumalai, J. F. Goodwin, D. M. Lucas, and C. J. Ballance, "High-rate, high-fidelity entanglement of qubits across an elementary quantum network," *Phys. Rev. Lett.*, vol. 124, p. 110501, Mar 2020. [Online]. Available: https://link.aps.org/doi/10.1103/PhysRevLett.124.110501

[35] M. Steiner, H. M. Meyer, C. Deutsch, J. Reichel, and M. Köhl, "Single ion coupled to an optical fiber cavity," *Physical review letters*, vol. 110, no. 4, p. 043003, 2013.

[36] M. Steiner, "A single ion inside a miniature cavity," Ph.D. dissertation, University of Cambridge, year = 2014, address = University of Cambridge,.

[37] J. Schmitz, H. M. Meyer, and M. Köhl, "Ultraviolet fabry-perot cavity with stable finesse under ultrahigh vacuum conditions," *Review of Scientific Instruments*, vol. 90, no. 6, p. 063102, 2019.

[38] T. Walker, K. Miyanishi, R. Ikuta, H. Takahashi, S. Vartabi Kashanian, Y. Tsujimoto, K. Hayasaka, T. Yamamoto, N. Imoto, and M. Keller, "Long-distance single photon transmission from a trapped ion via quantum frequency conversion," *Phys. Rev. Lett.*, vol. 120, p. 203601, May 2018. [Online]. Available: https://link.aps.org/doi/10.1103/PhysRevLett.120.203601

[39] E. Kassa, H. Takahashi, C. Christoforou, and M. Keller, "Precise positioning of an ion in an integrated paul trap-cavity system using radiofrequency signals," *Journal of Modern Optics*, vol. 65, no. 5-6, pp. 520–528, 2018. [Online]. Available: https://doi.org/10.1080/09500340.2017.1406158

[40] W. Paul and H. Steinwedel, "Notizen: Ein neues massenspektrometer ohne magnetfeld. zeitschrift für naturforschung a," *Zeitschrift für Naturforschung A*, vol. 8, pp. 448–450, 53. [Online]. Available: https://www.degruyter.com/view/j/zna.1953.8.issue-7/zna-1953-0710/zna-1953-0710.xml

[41] A. Riley-Watson, "A fibre-based single-photon source," Ph.D. dissertation, University of Sussex, year = 2012, address = University of Sussex,.

[42] D. Leibfried, R. Blatt, C. Monroe, and D. Wineland, "Quantum dynamics of single trapped ions," *Rev. Mod. Phys.*, vol. 75, pp. 281–324, Mar 2003. [Online]. Available: https://link.aps.org/doi/10.1103/RevModPhys.75.281

[43] E. Kassa, Ph.D. dissertation, University of Sussex, University of Sussex, 2017.

[44] E. D. Black, "An introduction to pound–drever–hall laser frequency stabilization," *American journal of physics*, vol. 69, no. 1, pp. 79–87, 2001.

[45] T. H. P. N. e. a. Gulati, G.K., "Fiber cavities with integrated mode matching optics," *Sci Rep*, vol. 7, no. 5556, 2017.

[46] J. Gallego, "Strong coupling between small atomic ensembles and an open fiber cavity," Ph.D. dissertation, University of Bonn, University of Bonn, 2017.

[47] D. Jones, "Lecture notes: Ubc physics 408: Optics (2010/11 term 2)," *Chapter 1: The Optical Cavity*, vol. vancouver, 2017.

[48] E. S. A, *Lasers*. University Science Books; Revised ed. edition, 1986.

[49] H. Takahashi, J. Morphew, F. Oručević, A. Noguchi, E. Kassa, and M. Keller, "Novel laser machining of optical fibers for long cavities with low birefringence," *Opt. Express*, vol. 22, no. 25, pp. 31 317–31 328, Dec 2014. [Online]. Available: http://www.opticsexpress.org/abstract.cfm?URI=oe-22-25-31317

[50] J. I. Cirac, S. J. van Enk, P. Zoller, H. J. Kimble, and H. Mabuchi, "Quantum communication in a quantum network," *Physica Scripta*, vol. T76, no. 1, p. 223, 1998. [Online]. Available: https://doi.org/10.1238%2Fphysica.topical.076a00223

[51] J. Alnis, A. Matveev, N. Kolachevsky, T. Wilken, T. Udem, and T. Hänsch, "Sub-hz line width diode lasers by stabilization to vibrationally and thermally compensated ule fabry-perot cavities," *arXiv preprint arXiv:0801.4199*, 2008.

[52] T. G. Ballance, "An ultraviolet fibre-cavity for strong ion-photon interaction," Ph.D. dissertation, University of Cambridge, Magdalene College, 2016.

[53] A. H. Nizamani and W. K. Hensinger, "Optimum electrode configurations for fast ion separation in microfabricated surface ion traps," *Applied Physics B*, vol. 106, no. 2, pp. 327–338, 2012.

[54] W.-B. Ji, J.-Y. Wan, H.-D. Cheng, and L. Liu, "A grooved planar ion trap design for scalable quantum information processing," *Chinese Physics B*, vol. 21, no. 6, p. 063701, jun 2012. [Online]. Available: https://doi.org/10.1088%2F1674-1056%2F21%2F6%2F063701

[55] C. Pearson, D. Leibrandt, W. S. Bakr, W. Mallard, K. Brown, and I. Chuang, "Experimental investigation of planar ion traps," *Physical Review A*, vol. 73, no. 3, p. 032307, 2006.

[56] M. A. Rowe, A. Ben-Kish, B. Demarco, D. Leibfried, V. Meyer, J. Beall, J. Britton, J. Hughes, W. M. Itano, B. Jelenkovic *et al.*, "Transport of quantum states and separation of ions in a dual rf ion trap," *arXiv preprint quant-ph/0205094*, 2002.

[57] W. Hensinger, S. Olmschenk, D. Stick, D. Hucul, M. Yeo, M. Acton, L. Deslauriers, C. Monroe, and J. Rabchuk, "T-junction ion trap array for two-dimensional ion shuttling, storage, and manipulation," *Applied Physics Letters*, vol. 88, no. 3, p. 034101, 2006.

[58] J. P. Home and A. M. Steane, "Electrode configurations for fast separation of trapped ions," *arXiv preprint quant-ph/0411102*, 2004.